Article

Pharmacological restoration of GTP hydrolysis by mutant RAS

https://doi.org/10.1038/s41586-024-08283-2

Received: 23 April 2024

Accepted: 24 October 2024

Published online: 30 October 2024

Open access

Check for updates

Antonio Cuevas-Navarro[1,7], Yasin Pourfarjam[1,7], Feng Hu[1], Diego J. Rodriguez[2], Alberto Vides[1], Ben Sang[1], Shijie Fan[1], Yehuda Goldgur[3], Elisa de Stanchina[4] & Piro Lito[1,2,5,6]✉

Approximately 3.4 million patients worldwide are diagnosed each year with cancers that have pathogenic mutations in one of three RAS proto-oncogenes (*KRAS, NRAS* and *HRAS*)[1,2]. These mutations impair the GTPase activity of RAS, leading to activation of downstream signalling and proliferation[3–6]. Long-standing efforts to restore the hydrolase activity of RAS mutants have been unsuccessful, extinguishing any consideration towards a viable therapeutic strategy[7]. Here we show that tri-complex inhibitors—that is, molecular glues with the ability to recruit cyclophilin A (CYPA) to the active state of RAS—have a dual mechanism of action: not only do they prevent activated RAS from binding to its effectors, but they also stimulate GTP hydrolysis. Drug-bound CYPA complexes modulate residues in the switch II motif of RAS to coordinate the nucleophilic attack on the γ-phosphate of GTP in a mutation-specific manner. RAS mutants that were most sensitive to stimulation of GTPase activity were more susceptible to treatment than mutants in which the hydrolysis could not be enhanced, suggesting that pharmacological stimulation of hydrolysis potentiates the therapeutic effects of tri-complex inhibitors for specific RAS mutants. This study lays the foundation for developing a class of therapeutics that inhibit cancer growth by stimulating mutant GTPase activity.

KRAS, NRAS and HRAS proteins hydrolyse GTP to GDP and control multiple cellular functions by cycling between an active (GTP bound) and an inactive (GDP bound) state[3–6]. These enzymes have a weak intrinsic GTPase activity, which is physiologically enhanced by GTPase-activating proteins (GAPs)[8–10]. RAS mutations impair the GTPase activity by preventing a catalytic arginine residue (R-finger) in GAPs from participating in hydrolysis or by failing to appropriately coordinate the water molecule involved in the nucleophilic attack[11–13]. On the basis of these observations, RAS mutants were historically thought to be constitutively activated in cancer. We have shown that most KRAS mutants are susceptible to inhibitors preferentially targeting their inactive state because they retain the ability to hydrolyse GTP in cancer cells[14–17]. Indeed, the GTPase activity of some KRAS mutants can be enhanced by atypical GAPs, which operate independently of a catalytic R-finger[16]. These findings prompt a search for pharmacological methods that could enhance mutant KRAS hydrolysis in an atypical manner.

In contrast to drugs targeting the inactive state, RAS inhibitors with preferential binding to the active state may modulate hydrolysis. Tri-complex inhibitors (TCIs) recruit cyclophilin A (CYPA) to the GTP-bound conformation of certain KRAS mutants in a covalent manner or multiple RAS variants in a reversible manner[18,19]. Early clinical data show a 43–50% response rate in patients with KRAS(G12C) mutant lung cancer treated with the G12C-selective covalent inhibitor RMC-6291[20] or an approximately 38% unconfirmed response rate in patients with KRAS(G12X) mutant lung cancer treated with the reversible multiselective inhibitor RMC-6236[21,22]. The mechanism that results in inhibition by covalent TCIs is straightforward: irreversible recruitment of CYPA to the active state of mutant KRAS prevents binding to effector proteins like CRAF and PI3K, thereby inactivating downstream signalling. However, the exact mechanism of reversible TCIs and, particularly, how these drugs offer durable inhibition of downstream signalling when CYPA can, in principle, dissociate from active RAS remains unclear.

Variation in RAS–CYPA complex formation

We began by testing the ability of reversible active-state selective TCIs (Extended Data Fig. 1a–c) to induce a complex between CYPA and various common RAS mutants found in cancer. HEK293T cells were engineered to express these proteins as part of a split luciferase complementation reporter. The interaction between RAS and CYPA reconstituted the luciferase enzyme, permitting the quantification of binding in live cells. As shown in Fig. 1a and Extended Data Fig. 2a, increasing concentrations of the clinical agent RMC-6236, or its equipotent analogue RMC-7977, led to a dose-dependent increase in KRAS–CYPA interaction. However, the magnitude of the complex differed across variants: wild-type (WT) and G12X mutants had a low-level interaction, G13X, K117N and A146X mutants varied between intermediate to high-level binding, and Q61X mutants had the highest binding. This analysis revealed a significant difference in maximal CYPA binding between G12X and non-G12X variants, despite comparable

[1]Human Oncology and Pathogenesis Program, Memorial Sloan Kettering Cancer Center, New York, NY, USA. [2]Tri-Institutional MD-PhD Program, Weill Cornell Medical College and Rockefeller University and Memorial Sloan Kettering Cancer Center, New York, NY, USA. [3]Structural Biology Program, Memorial Sloan Kettering Cancer Center, New York, NY, USA. [4]Antitumor Assessment Core Facility, Memorial Sloan Kettering Cancer Center, New York, NY, USA. [5]Department of Medicine, Memorial Sloan Kettering Cancer Center, New York, NY, USA. [6]Department of Medicine, Weill Cornell Medical College, New York, NY, USA. [7]These authors contributed equally: Antonio Cuevas-Navarro, Yasin Pourfarjam. ✉e-mail: litop@mskcc.org

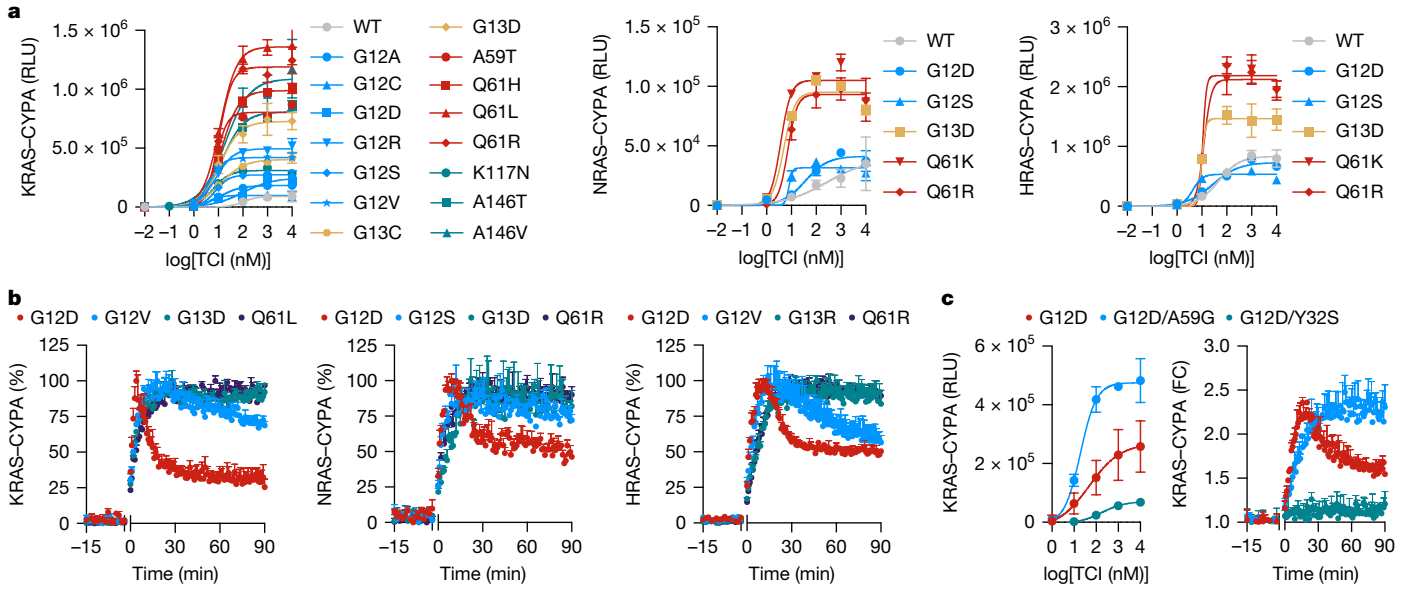

Fig. 1 | Reversible TCI with differential binding capacity for RAS mutants. **a**, Live cells expressing a split luciferase reporter detecting the complex between CYPA and the indicated KRAS (left), NRAS (middle) or HRAS (right) variants were treated with a TCI (RMC-7977) for 2 h. **b**, As described in **a**, but live cells were assayed over time, either before or after treatment with RMC-7977 (100 nM, added at t_0). **c**, The effect of the indicated KRAS mutations on drug-induced complex formation between KRAS and CYPA in live cells. Y32S was used a negative control, as this residue has been shown to be important for tri-complex formation[18,19]. For **a**–**c**, $n = 3$. Data are mean ± s.e.m. Unless otherwise indicated, n denotes biological replicates. FC, fold change.

expression levels between the mutants (Extended Data Fig. 2b–d). A similar pattern in CYPA complex formation was observed for NRAS or HRAS mutants (Fig. 1a).

We next tested the kinetics of drug-induced complex formation and found that KRAS(Q61) mutants form a relatively stable complex with CYPA in response to RMC-7977 treatment (at least for the duration of the experiment; Fig. 1b and Extended Data Fig. 2e,f). By contrast, G12D and G12V KRAS mutants displayed a bimodal effect, where initial binding was followed by dissociation (of a variable rate, see below). Again, similar findings were observed for these substitutions in HRAS and NRAS (Fig. 1b and Extended Data Fig. 2g,h). Co-targeting upstream regulators, such as EGFR, SHP2 and SOS1, diminished the steady-state level of the KRAS(G12D)–CYPA complex (Extended Data Fig. 2i,j). As expected, RMC-7977 disrupted the interaction between GMPPNP-loaded mutant KRAS and the RAS-binding domain (RBD) of CRAF, and had little if any effect on SOS1-mediated nucleotide exchange of GDP for GTP (Extended Data Fig. 1b,c).

Stimulation of mutant RAS GTPase activity

The rapid dissociation (Fig. 1b) and the lower apparent steady-state CYPA complex formation (Fig. 1a and Extended Data Fig. 2b) in KRAS(G12X)-expressing cells treated with RMC-7977 are puzzling observations. They suggest that some reversible TCIs have additional mechanistic features that enable inhibition besides simply recruiting CYPA to displace effectors from active RAS. Suspecting that one such feature might be the modulation of hydrolysis, we tested the effect of the hydrolysis transition-state mutation A59G[23,24] on the KRAS(G12D)–CYPA complex induced by RMC-7977. The KRAS(G12D/A59G) double mutant had a higher magnitude of complex formation and did not exhibit dissociation over a 90 min treatment interval, in contrast to the effect of treatment on singly mutated KRAS(G12D) (Fig. 1c).

In biochemical hydrolysis assays with purified proteins, neither RMC-7977 nor CYPA alone led to an increase in GTP hydrolysis by WT or G12D mutant KRAS (Fig. 2a). However, CYPA combined with RMC-7977 led to a dose-dependent increase in the level of PO_4 released by KRAS. The reaction reached a maximum rate at approximately 5 μM CYPA–RMC-7977 (Extended Data Fig. 3a). Notably, the hydrolysis-inducing effect on KRAS WT was considerably weaker than that on KRAS(G12D) (Fig. 2a). Moreover, the rate of CYPA–RMC-7977-stimulated hydrolysis by KRAS(G12D) was slower than that of NF1-stimulated hydrolysis by WT KRAS.

We next compared the effects of CYPA–RMC-7977 in stimulating hydrolysis by other RAS variants (Fig. 2b and Extended Data Fig. 3b–d for KRAS, NRAS and HRAS mutants, respectively). The stimulation of hydrolysis varied across mutants, being most pronounced for the G12D, G12A, G12S, G12V, G12C and G12R mutants (listed by order of magnitude) and was nearly undetectable for the Q61X or A59T mutants. The KRAS(G13X) and KRAS(K117N) mutants had an intermediate effect. This trend was again conserved across RAS isoforms (and was inversely related to the magnitude of RMC-7977-induced CYPA binding by these mutants, as evidenced in Fig. 1a). An orthogonal assay that measures the loss of [γ^{33}P]GTP during hydrolysis showed that CYPA bound to RMC-7977 similarly enhanced GTP hydrolysis by KRAS(G12D) but not by the KRAS(G12D/A59G) double mutant (Fig. 2c). CYPA bound to RMC-6236 induced similar levels of GTP hydrolysis by KRAS(G12D) compared to CYPA bound to RMC-7977 (Extended Data Fig. 4a,b). No induction of KRAS(G12C)-mediated hydrolysis was observed for CYPA bound to RMC-4998—a G12C-selective covalent TCI (Extended Data Fig. 4c).

We next examined whether drug-bound CYPA stabilized the transition state of the hydrolysis reaction. The transition state was modelled using a mixture of GDP and AlF_3, with the latter having previously been described to mimic the γ-phosphate released during the hydrolysis reaction[25]. To this end, KRAS variants were loaded with mant-GDP·AlF_3 and then mixed with drug-bound CYPA. The conformational change caused by binding to the transition state of KRAS was determined by the change in the fluorescence emission spectrum of mant-GDP. In agreement with the data above, CYPA–RMC-7977 led to a dose-dependent increase in transition-state binding with only a little effect by either RMC-7977 or CYPA alone (Fig. 2d and Extended Data Fig. 4d). Minimal such binding was observed for the KRAS mutants with minimal tri-complex-induced hydrolysis (Fig. 2e; Q61L and G13D).

Mechanism enabling GTPase activation

Having established the variable hydrolysis-inducing abilities of TCIs across different RAS mutants, we turned our attention to the underlying

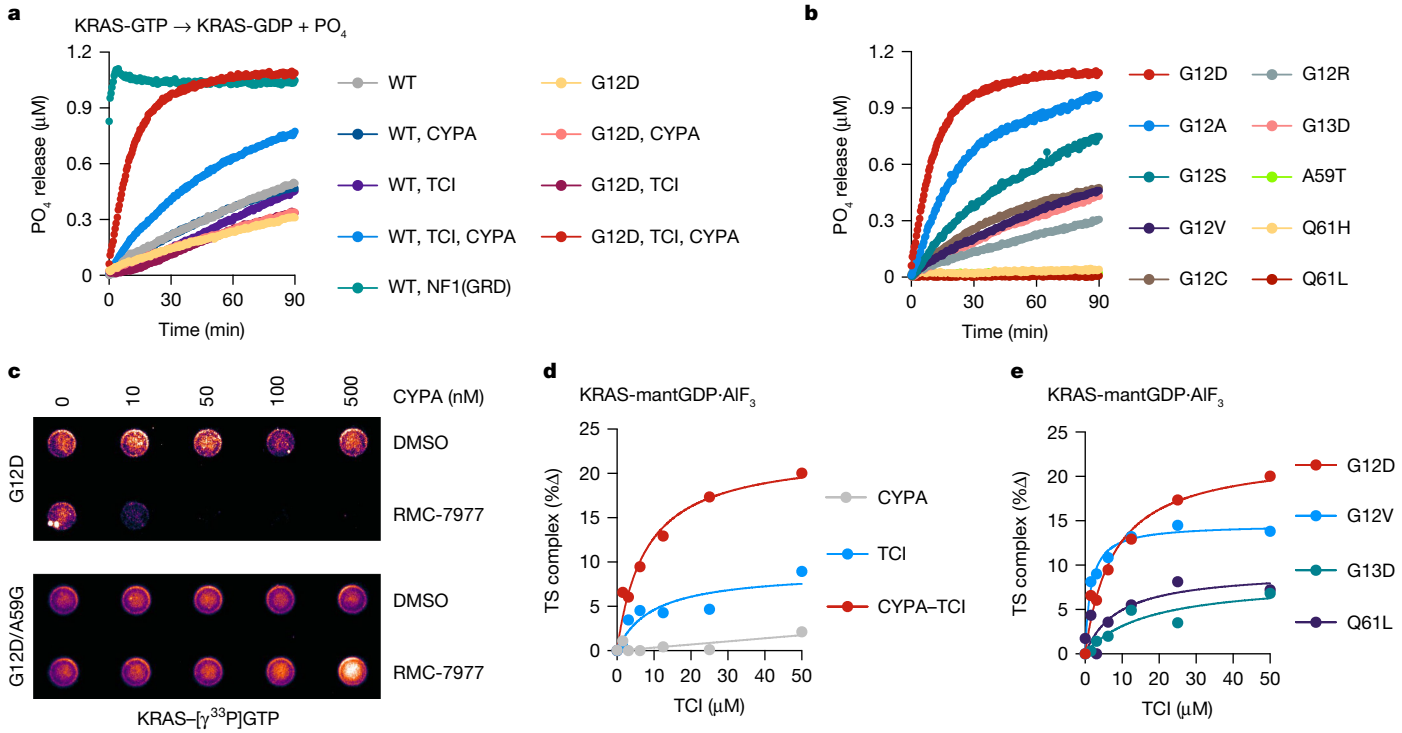

Fig. 2 | Pharmacological restoration of GTP hydrolysis by mutant RAS. **a**, GTP hydrolysis by recombinant WT or mutant KRAS was assayed using an orthophosphate sensor protein, either under intrinsic conditions or in the presence of the indicated agents. The GAP domain of NF1 (GRD), which enhances GTP hydrolysis by WT (but not mutant) KRAS, was used as a control. **b**, The effect of drug-bound CYPA on enhancing GTP hydrolysis by the indicated KRAS mutants. See also Extended Data Fig. 3. **c**, The effect of CYPA or CYPA–RMC-7977 complex on the ability of KRAS(G12D) to hydrolyse [γ^{33}P]GTP. **d**, Purified KRAS(G12D) loaded with mant-GDP (mGDP) and AlF_3 was reacted with increasing concentrations of drug-bound CYPA. The transition state (TS) complex was detected by the change in fluorescence and reported as the change in the area under the curve. **e**, As in **d**, but with the indicated KRAS variants. A representative experiment of $n = 2$ independent experiments for each KRAS variant is shown in **a**–**e**.

structural mechanism responsible for this effect. The complexes of drug-bound CYPA and various KRAS mutants loaded with GMPPNP (modelling the ground state) or with GDP·AlF_3 (modelling the transition state) were isolated using size-exclusion chromatography and crystallized as described in the Methods (Extended Data Fig. 5a–e).

In the KRAS(G12C/S/A) transition states, AlF_3 and the nucleophilic water molecule faced outward and coordinated between Gln61 and Thr35 (Fig. 3a–c and Extended Data Fig. 6a,b). CYPA–RMC-7977 adopted a conformation that was nearly identical to that observed in the ground state with a portion of the indole and thiazole rings of RMC-7977 stabilizing switch II residues Met67, Tyr64, Glu63 and Gln61 (Extended Data Fig. 6c). The key difference between the GMPPNP- and AlF_3-bound structures of these mutants was the rotation of the Gln61 side chain towards AlF_3 and the nucleophilic water, with the carbonyl of the Gln61 amide pointing towards the later (Fig. 3a–c and Extended Data Fig. 6c (inset)). Many of the features of the KRAS(G12C/S/A) tri-complex transition states, including the positioning and the geometry of GDP·AlF_3·H_2O_{nu}, were similar to those observed in WT HRAS in complex with the canonical GAP RASA1[12] (Extended Data Fig. 6d). However, the notable absence of the key catalytic arginine residue in the former suggests that tri-complex-assisted hydrolysis occurs through a mechanism that is distinct from that of canonical RAS GAPs.

Despite repeated attempts, we were unable to acquire a KRAS(G12D)–GDP·AlF_3 tri-complex structure with an electron density that could be attributed to AlF_3·H_2O_{nu} in the typical outward position (that is, between Gln61 and Thr35). However, these structures were distinct from the GMPPNP-bound structures in that the mutated aspartate had shifted to an inward orientation whereby its carboxyl group participated in an H-bond network involving the backbone of Gly60 and the side chain of Gln61, partly occupying the typical space of AlF_3 and interacting with a water molecule positioned between Gln61 and Thr35 (Fig. 3d). By comparison, the mutant cysteine, alanine and serine side chains did not extend sufficiently inward to interfere with the positioning of AlF_3 or to interact with the nucleophilic water molecule (Fig. 3a–c). In one of the KRAS(G12D) tri-complex protomer pairs, the AlF_3·H_2O_{nu} moiety could be most plausibly modelled in an inward orientation, between the mutant aspartate and the side chain of Lys16 (Fig. 3e). The absence of any existing transition-state structures for mutant RAS makes it hard to determine the significance of the alternatively placed AlF_3 in the KRAS G12D tri-complex structure. Nevertheless, we also identified two possible occupancies for the γ-phosphate in one of the GMPPNP-bound KRAS(G12D) tri-complex pairs (Extended Data Fig. 6e): the typical outward orientation and an inward orientation, that was similar to that putatively occupied by the AlF_3 moiety in Fig. 3e. Although dedicated studies are needed to clarify the positioning of AlF_3 in the G12D transition state, our data clearly demonstrate the rotation of the mutant aspartate towards the catalytic core of KRAS (Fig. 3f) and suggest a role in directly coordinating the nucleophilic water molecule involved in hydrolysis (see below).

Validation of key mechanistic features

The structural features above suggest that Gln61 has a conserved role in the tri-complex-stimulated hydrolysis of the various Gly12 mutants. We therefore tested the effect of a Gln61 mutation on GTP hydrolysis and on the stability of the cellular KRAS–CYPA complex. Introducing the Q61L mutation alongside KRAS(G12D) or KRAS(G12V) led to diminished GTP hydrolysis (Fig. 4a) and a higher capacity for CYPA binding with little, if any, dissociation as compared to KRAS with a single G12D or G12V mutation (Fig. 4b,c).

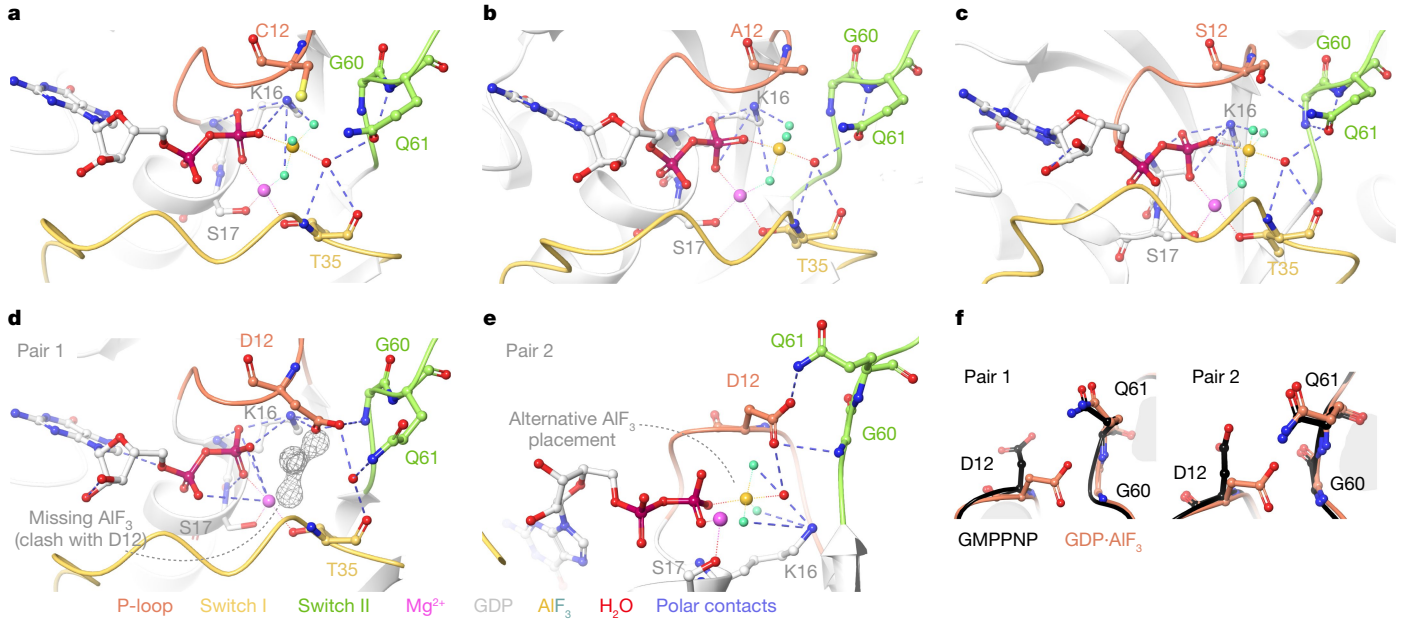

Fig. 3 | The structural basis for enhanced GTP hydrolysis by mutant KRAS. **a**–**c**, The key features of the KRAS mutants G12C (**a**), G12S (**b**) and G12A (**c**) loaded with GDP·AlF_3 in a complex with CYPA–RMC-7977. **d**,**e**, Conformations observed in GDP·AlF_3-loaded KRAS(G12D) tri-complex pairs. The missing AlF_3 in the typical position due to a steric clash with the mutant Asp12 side chain (**d**) and a plausible alternative placement (**e**) are shown. **f**, Inward rotation of the mutant aspartate in the GDP·AlF_3-loaded KRAS(G12D) tri-complex protomer pairs, as compared to the GMPPNP-loaded conformation.

We next examined whether the carboxyl group of aspartate-12 enables an additional acceleration of tri-complex-induced hydrolysis in a mutant-specific manner. To test this possibility, we substituted the aspartate for an asparagine, which differs only in that it contains an amide instead of a carboxyl group in its side chain (Fig. 4d). This lowered the hydrolysis rate to a level slightly higher than that of G12V (Fig. 4e) and attenuated the dissociation of the KRAS–CYPA complex in live cells (Fig. 4f). By comparison, substitution of Asp12 for glutamate (which also contains a carboxyl group) had a little effect on GTP hydrolysis or dissociation (Fig. 4e,f), whereas its substitution for glutamine (which contains an amide) again attenuated GTP hydrolysis and dissociation, a finding that is indicative of diminished tri-complex-induced hydrolysis in cells.

We also examined other amino acid residues that were deemed to be important for the appropriate orientation of Gln61 from the structures above. The secondary mutations G60A or E63A each attenuated the GTPase-enhancing effect of the CYPA–TCI binary complex on KRAS(G12D) (Extended Data Fig. 7a,b). In live cells, G60A and E63A led

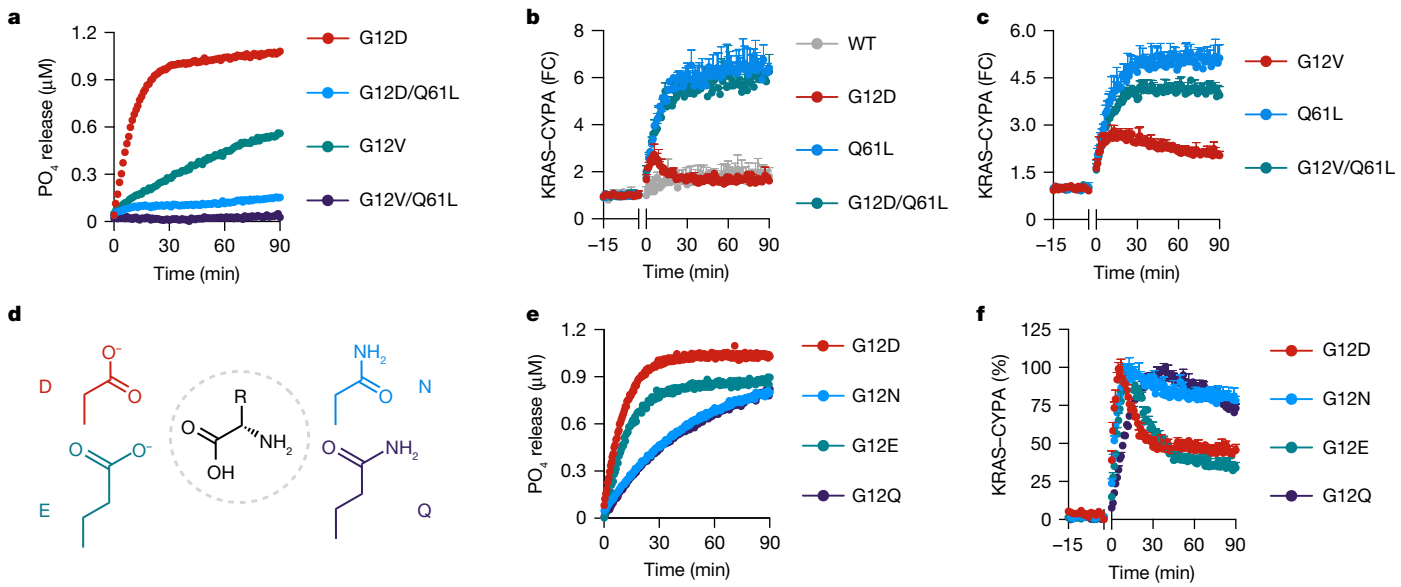

Fig. 4 | KRAS amino acids with a catalytic effect on tri-complex-induced hydrolysis. **a**, The effect of the CYPA–RMC-7977 complex on GTP hydrolysis by the indicated KRAS variants. A representative experiment of $n = 2$ independent experiments is shown. **b**,**c**, Detection of RMC-7977-induced complex formation between CYPA and the KRAS(G12D) (**b**) or KRAS(G12V) (**c**) mutant in live cells. $n = 3$ biological replicates. Data are mean ± s.e.m. **d**, The structures of the isosteric amino acid substitutions used in **e** and **f**. **e**, The effect of CYPA–RMC-7977 complex on GTP hydrolysis by the indicated KRAS mutants. A representative experiment of $n = 2$ independent experiments is shown. **f**, Detection of RMC-7977-induced complex formation between CYPA and the indicated KRAS mutants in live cells. $n = 3$ biological replicates. Data are mean ± s.e.m.

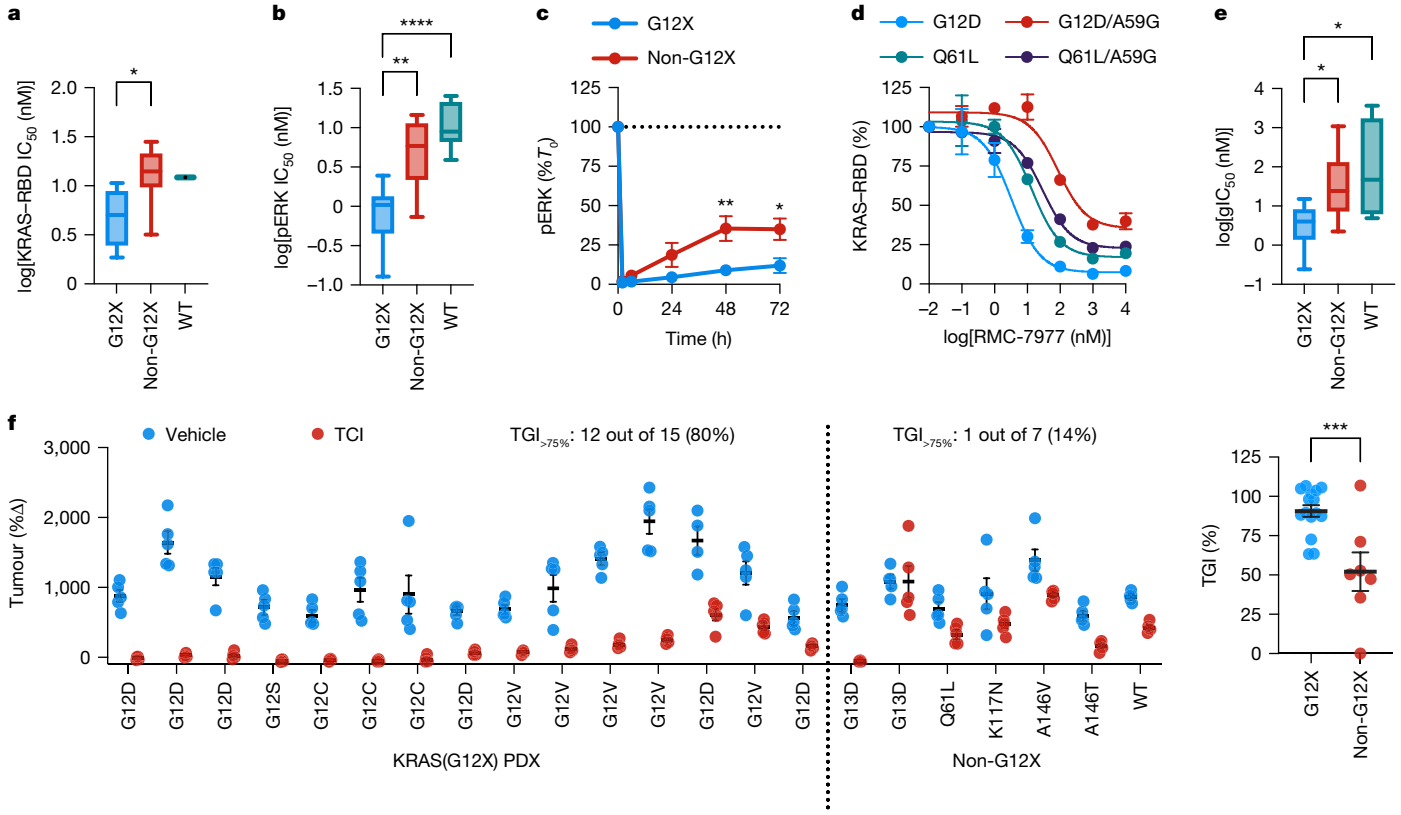

Fig. 5 | Implications of stimulating GTP hydrolysis on oncogenic KRAS inhibition. a, Live cells expressing a split luciferase reporter detecting the complex between the CRAF RBD and WT ($n = 1$), G12X (n = 6) or non-G12X ($n = 9$) KRAS variants (n denotes distinct variants) were treated with increasing concentrations of RMC-7977. The half-maximal inhibitory concentration (IC_{50}) is shown. Statistical analysis was performed using a two-tailed t-test; $^{*}P = 0.0107$. **b**, Cell lines containing the indicated KRAS variants were treated with increasing concentrations of RMC-7977 for 2 h to determine the effect on pERK using immunoblotting and densitometry. $n = 7, 10$ and 7 cell lines for the WT, G12X and non-G12X groups, respectively. Statistical analysis was performed using one-way ANOVA followed by Dunnett's test; $^{**}P = 0.0018$, $^{****}P = 0.0001$. **c**, Models containing G12D, G12V, G13D or Q61X mutant KRAS ($n = 4$ cell lines per allele) were treated as shown and the cell extracts were assayed to determine the effect on pERK inhibition over time. Data are mean ± s.e.m. Statistical analysis was performed using two-tailed t-tests; $^{*}P = 0.015$, $^{**}P = 0.008$. **d**, The interactions between the CRAF RBD and the indicated KRAS mutants in cells that were treated with RMC-7977 for 2 h as described in **a**. **e**, Cells were treated with increasing concentrations of RMC-7977 for 72 h to determine the effect on viability using ATP glow. $n = 4, 12$ and 9 for WT, G12X and non-G12X, respectively. The half-maximal growth inhibitory concentration (gIC50) is shown. Statistical analysis was performed using one-way ANOVA followed by Dunnett's test; $^{*}P = 0.0018$. **f**, Mice bearing PDX models containing either a G12X ($n = 15$) or a non-G12X ($n = 7$) KRAS mutation were treated with vehicle or RMC-7977 to determine the effect on tumour growth (left). $n = 4$ or 5 animals per treatment arm. Data are mean ± s.e.m. Right, tumour growth inhibition (TGI) by KRAS mutant groups. Data are mean ± s.e.m. Statistical analysis was performed using a two-tailed t-test; $^{***}P = 0.0009$. For **a**, **b** and **e**, the box plots show the median (centre line), interquartile range (box limits) and Tukey whiskers.

to either a loss of dissociation and/or to more binding, as compared to the KRAS(G12D) single mutant (Extended Data Fig. 7c,d).

Implications for mutant KRAS inhibition

Inducing hydrolysis may attenuate the inhibition of downstream signalling by TCIs because it results in dissociation of CYPA from mutant KRAS, with mutant KRAS then being susceptible to reactivation and engagement of effector signalling. Alternatively, the effect on hydrolysis may be an additional mechanistic feature enabling stronger signalling inhibition by some reversible TCIs. To test these possibilities, we compared the effects of RMC-7977 treatment on signalling inhibition in models containing KRAS(G12X) mutations, the hydrolysis of which can be enhanced by drug-bound CYPA, and in models containing non-G12X KRAS mutations, which had a minimal (if any) enhancement effect on hydrolysis.

We tested the effect of treatment on the interaction of KRAS with the CRAF RBD in live cells, which is a proxy for KRAS activation (Fig. 5a and Extended Data Fig. 8a,b). On average, treatment with RMC-7977 led to a deeper KRAS inactivation in cells expressing KRAS(G12X) mutants (that is, G12D/V/C/S/A/R), as compared to cells expressing non-G12X mutants (G13C/D, Q61H/L, K117N and A146T). In agreement with these results, cancer cells containing a KRAS(G12X) mutation had a more potent (Fig. 5b and Extended Data Fig. 8c) and durable (Fig. 5c and Extended Data Fig. 9a,b) inhibition of ERK signalling compared with models containing a non-G12X mutation. These effects were apparent despite KRAS(G12X) mutants having, on average, a lower steady-state drug-induced CYPA interaction in cells compared with non-G12X mutants (Extended Data Fig. 2b). Moreover, cells containing G12X or non-G12X KRAS mutations had a similar pattern of phosphorylated ERK (pERK) inhibition when treated with an inactive state selective pan-KRAS inhibitor that does not stimulate GTP hydrolysis (Extended Data Fig. 9c,d). We next examined whether the mutant-specific effects of hydrolysis-inducing TCIs could be attributed to the selective enhancement of mutant KRAS GTPase activity. Indeed, introducing secondary mutations that block TCI-stimulated GTP hydrolysis (such as Q61L or A59G) attenuated the effect of RMC-7977 treatment on KRAS(G12D) (which is susceptible to TCI-induced hydrolysis), but not its effect on G13D- or Q61L-mutant KRAS (of which the hydrolysis could not be stimulated by TCIs; Fig. 5d and Extended Data Fig. 8d).

We next assessed the effect of reversible TCI treatment on KRAS-driven tumour growth. Treatment with RMC-7977 elicited a

more potent anti-proliferative effect in G12X-mutant cells compared with WT and non-G12X mutant cells (Fig. 5e). As expected, co-targeting upstream nucleotide-exchange factors (either through SOS1 or SHP2 inhibition) enhanced the antiproliferative effect of RMC-7977 in KRAS(G12X) mutants, but not in models containing non-G12X KRAS mutations (Extended Data Fig. 9e). The antitumour activity of RMC-7977 in mice bearing patient-derived xenograft (PDX) models with a KRAS(G12X) mutation was again more pronounced than that in models with non-G12X mutations (Fig. 5f). The data therefore suggest that the ability of some active-state-selective TCIs to stimulate GTP hydrolysis is a key mechanistic feature that contributes to effective suppression of oncogenic RAS signalling in a mutant-RAS-specific manner.

Discussion

Over the past four decades, efforts to pharmacologically restore the hydrolase activity of mutant RAS have been unsuccessful, curtailing its evaluation as a potential therapeutic strategy[7]. Here we report the identification of a drug–protein complex that enhances GTP hydrolysis by mutant RAS. Our study shows that some TCIs, that is, molecular glues that recruit CYPA to the active (or GTP-loaded) conformation of RAS, can also enhance the ability of RAS mutants to hydrolyse GTP, an effect that was most evident in RAS Gly12 mutants.

Drug-bound CYPA (but neither drug nor CYPA alone) enhanced hydrolysis through an atypical mechanism by stabilizing the transition state in the absence of a catalytic arginine residue (which is present in GAPs that inactivate WT but not mutant RAS). The structural and functional studies reported above suggest that the drug–CYPA complexes interact with switch II residues, leading to the rotation of Gln61 in a hydrolysis-competent conformation. This mechanistic feature was conserved across the G12X mutants for which the transition state analogue structures were evaluated here. The carboxyl group of the mutant aspartate provides a fortuitous additive feature leading to further acceleration for this particular variant. The data suggest that the mutant aspartate either acts as a base making the adjacent water molecule more nucleophilic, or its negative charge enables interactions that affect the position of the γ-phosphate, enabling its faster release during hydrolysis.

The conversion of RAS–GTP to RAS–GDP in cells could be observed by the dissociation of GTP-dependent RAS–CYPA tertiary complexes. Indeed, the ability to induce hydrolysis explains the lower RMC-7977-induced CYPA complex formation by RAS(G12X) mutants: once hydrolysis is complete, RAS assumes its GDP-bound state, leading to dissociation of the CYPA–RMC-7977–RAS tri-complex. However, despite lowering the levels of steady-state binding in G12X mutants, stimulation of hydrolysis was correlated with a more pronounced and durable inactivation downstream signalling and tumour growth. The antitumour effect observed in some non-G12X mutant models is not surprising, considering that TCIs exert an inhibitory effect on mutant KRAS, even in the absence of GTP hydrolysis, by blocking interactions with its effector proteins.

Together, these data argue that some reversible TCIs inactivate mutant RAS in a bimodal manner by preventing effectors from being recruited to the active state of RAS and/or by enhancing the ability of RAS mutants to hydrolyse GTP leading to their inactivation. Which of these effects is predominantly responsible for target inhibition in cancer cells is likely to vary across mutants, depending on their association and dissociation rates for binding to the drug–CYPA binary complex, the catalytic efficiency of hydrolysis as well as context-dependent factors (such as, for example, the proportion of GTP-loaded RAS in cells). Nevertheless, whereas steric occlusion of effector binding is a mechanistic feature that is shared across WT and mutant RAS variants, the ability to induce hydrolysis is more prominent in KRAS(G12X) mutants. Overall, our work lays the groundwork for the future development of more-effective small-molecule enhancers of GTPase activity, aiming to pharmacologically reverse the catalytic defect imposed by RAS mutations found in cancer.

Online content

Any methods, additional references, Nature Portfolio reporting summaries, source data, extended data, supplementary information, acknowledgements, peer review information; details of author contributions and competing interests; and statements of data and code availability are available at https://doi.org/10.1038/s41586-024-08283-2.

1. Prior, I. A., Hood, F. E. & Hartley, J. L. The frequency of Ras mutations in cancer. *Cancer Res.* **80**, 2969–2974 (2020).
2. Punekar, S. R., Velcheti, V., Neel, B. G. & Wong, K.-K. The current state of the art and future trends in RAS-targeted cancer therapies. *Nat. Rev. Clin. Oncol.* **19**, 637–655 (2022).
3. Malumbres, M. & Barbacid, M. RAS oncogenes: the first 30 years. *Nat. Rev. Cancer* **3**, 459–465 (2003).
4. Hobbs, G. A., Der, C. J. & Rossman, K. L. RAS isoforms and mutations in cancer at a glance. *J. Cell Sci.* **129**, 1287–1292 (2016).
5. Simanshu, D. K., Nissley, D. V. & McCormick, F. RAS proteins and their regulators in human disease. *Cell* **170**, 17–33 (2017).
6. Kim, D., Xue, J. Y. & Lito, P. Targeting KRAS(G12C): from inhibitory mechanism to modulation of antitumor effects in patients. *Cell* **183**, 850–859 (2020).
7. Stephen, A. G., Esposito, D., Bagni, R. K. & McCormick, F. Dragging Ras back in the ring. *Cancer Cell* **25**, 272–281 (2014).
8. Trahey, M. & McCormick, F. A cytoplasmic protein stimulates normal N-ras p21 GTPase, but does not affect oncogenic mutants. *Science* **238**, 542–545 (1987).
9. Xu, G. et al. The catalytic domain of the neurofibromatosis type 1 gene product stimulates *ras*GTPase and complements *ira*mutants of *S. cerevisiae*. *Cell* **63**, 835–841 (1990).
10. Bollag, G. & McCormick, F. Differential regulation of rasGAP and neurofibromatosis gene product activities. *Nature* **351**, 576–579 (1991).
11. Ahmadian, M. R., Stege, P., Scheffzek, K. & Wittinghofer, A. Confirmation of the arginine-finger hypothesis for the GAP-stimulated GTP-hydrolysis reaction of Ras. *Nat. Struct. Biol.* **4**, 686–689 (1997).
12. Scheffzek, K. et al. The Ras-RasGAP complex: structural basis for GTPase activation and its loss in oncogenic Ras mutants. *Science* **277**, 333–338 (1997).
13. Vetter, I. R. & Wittinghofer, A. The guanine nucleotide-binding switch in three dimensions. *Science* **294**, 1299–1304 (2001).
14. Lito, P., Solomon, M., Li, L. S., Hansen, R. & Rosen, N. Allele-specific inhibitors inactivate mutant KRAS G12C by a trapping mechanism. *Science* **351**, 604–608 (2016).
15. Xue, J. Y. et al. Rapid non-uniform adaptation to conformation-specific KRAS(G12C) inhibition. *Nature* **577**, 421–425 (2020).
16. Li, C. et al. The G protein signaling regulator RGS3 enhances the GTPase activity of KRAS. *Science* **374**, 197–201 (2021).
17. Kim, D. et al. Pan-KRAS inhibitor disables oncogenic signalling and tumour growth. *Nature* **619**, 160–166 (2023).
18. Schulze, C. J. et al. Chemical remodeling of a cellular chaperone to target the active state of mutant KRAS. *Science* **381**, 794–799 (2023).
19. Holderfield, M. et al. Concurrent inhibition of oncogenic and wild-type RAS-GTP for cancer therapy. *Nature* https://doi.org/10.1038/s41586-024-07205-6 (2024).
20. Jänne, P. A. et al. Abstract PR014: preliminary safety and anti-tumor activity of RMC-6291, a first-in-class, tri-complex KRASG12C(ON) inhibitor, in patients with or without prior KRASG12C(OFF) inhibitor treatment. *Mol. Cancer Ther.* **22**, PR014 (2023).
21. Arbour, K. C. et al. 652O preliminary clinical activity of RMC-6236, a first-in-class, RAS-selective, tri-complex RAS-MULTI(ON) inhibitor in patients with KRAS mutant pancreatic ductal adenocarcinoma (PDAC) and non-small cell lung cancer (NSCLC). *Ann. Oncol.* **34**, S458 (2023).
22. Jiang, J. et al. Translational and therapeutic evaluation of RAS-GTP inhibition by RMC-6236 in RAS-driven cancers. *Cancer Discov.* **14**, 994–1017 (2024).
23. Hall, B. E., Bar-Sagi, D. & Nassar, N. The structural basis for the transition from Ras-GTP to Ras-GDP. *Proc. Natl Acad. Sci. USA* **99**, 12138–12142 (2002).
24. Margarit, S. M. et al. Structural evidence for feedback activation by Ras·GTP of the Ras-specific nucleotide exchange factor SOS. *Cell* **112**, 685–695 (2003).
25. Wittinghofer, A. Signaling mechanistics: aluminum fluoride for molecule of the year. *Curr. Biol.* **7**, R682–R685 (1997).

Methods

Inhibitors

The TCIs RMC-7977, RMC-4998, RMC-6236 and RMC-4550 were provided by Revolution Medicines. Gefitinib, BI-3406 and Trametinib were purchased from Selleckchem.

Protein expression and purification

Codon-optimized human RAS (HRAS, NRAS, KRAS, amino acids 1–169), CYPA and NF1 GRD (amino acids 1198–1530) constructs were cloned into pET expression vectors with an N-terminal hexahistidine (His_6) (Addgene, 29653) or His_6–GST tag (Addgene, 29655). Expression of each construct was induced with 0.2 mM isopropyl-β-D-thiogalactoside in *Escherichia coli* BL21 (DE3) cells cultured in Terrific Broth medium at 18 °C for 16–20 h. For His_6-tagged proteins, BL21 cells were lysed by sonication in lysis buffer (50 mM Tris-HCl pH 7.5, 150 mM NaCl, 10% glycerol, 30 mM imidazole, 1 mM benzamidine, 1 mM phenylmethylsulfonyl fluoride). For His_6–GST-tagged proteins, BL21 cells were lysed by sonication in lysis buffer (50 mM Tris-HCl pH 7.5, 150 mM NaCl, 10% glycerol, 1 mM benzamidine, 1 mM phenylmethylsulfonyl fluoride). Cleared lysates were subjected to affinity purification using Ni Sepharose 6 Fast Flow resin (Cytiva) or Glutathione Sepharose 4B (Cytiva). His-tagged proteins were eluted in 300 mM imidazole and GST-tagged proteins were eluted in 20 mM reduced glutathione (pH 8.8). The eluted fractions were subjected to a second round of purification by size-exclusion chromatography (SEC) on the Superdex 75 10/300 GL column (Cytiva) equilibrated with SEC buffer (25 mM HEPES pH 7.5, 150 mM NaCl, 1 mM TCEP). Fractions containing the protein of interest were pooled, concentrated and frozen in liquid nitrogen. For the purification of RAS proteins, all buffers were supplemented with 2 mM $MgCl_2$. For crystallography, His-tagged KRAS and CYPA were purified over Ni Sepharose 6 followed by overnight cleavage of the His tag by Tobacco Etch Virus (TEV) protease (1:20, TEV: KRAS, CYPA) at 4 °C. The cleaved His tag and TEV were removed by another round of Ni Sepharose 6. KRAS and CYPA were then further purified by SEC on the Superdex 75 10/300 GL column pre-equilibrated with buffer comprising 12.5 mM HEPES pH 7.5, 75 mM NaCl.

Crystallography

Ground- and transition-state mimetic complexes and crystallization. For the formation of the ground-state complex between KRAS, CYPA and RMC-7977, 250 μM of GMPPNP-loaded KRAS was mixed with 500 μM CYPA and 750 μM RMC-7977 in binding buffer (12.5 mM HEPES pH 7.4, 75 mM NaCl and 5 mM $MgCl_2$). The reaction was then incubated for 1 h on ice before injection into the Superdex 75 10/300 GL column pre-equilibrated with binding buffer. The fractions containing the complex were collected and concentrated to 15 mg ml^{-1} using a 30 kDa MWCO Centricon (Millipore). For the formation of the transition-state mimetic complex, 250 μM of GDP-loaded KRAS in transition state buffer (12.5 mM HEPES pH 7.4, 75 mM NaCl, 2 mM $MgCl_2$, 2 mM $AlCl_3$ and 100 mM NaF) was incubated with 500 μM CYPA and 750 μM RMC-7977 for 1 h on ice. The complex was then isolated by gel filtration using the Superdex 75 10/300 GL column pre-equilibrated with transition-state buffer. Initial crystal screening was performed at 18 °C in 96-well sitting drop plates using 0.5 μl protein complex and 0.5 μl mother liquor over 60 μl sparse matrix. Crystals appeared a day later in solutions consisting of 0.1 M Tris-HCl pH 8.5 and 20–25% PEG 8000 and PEG 10000. Selected crystals were flash-frozen in cryoprotectant consisting of mother liquor supplemented with 25% glycerol.

Data collection, structure determination and analysis. All datasets were collected at the NSLS II 17-ID-2 (FMX) beamline and processed using HKL2000[26]. The structure of GDP·AlF_3-loaded KRAS(G12D) was solved in Phenix phaser[27] using crystal structures of KRAS(G12D) (Protein Data Bank (PDB): 5US4)[28] and CYPA (PDB: 3K0N)[29] as search models. A strong difference electron density for RMC-7977 was observed. The restrain for RMC-7977 was generated in AceDRG[30] in the CCP4 package and energy minimized in Phenix eLBOW[31]. Models were built in Coot[32] and refined in phenix.refine[33]. Other structures were determined in a similar manner, using the G12D tri-complex structure as the search model in Phenix phaser. For GMPPNP-bound structures, the nucleotide was fitted into the electron density using the Real Space Refine option in the coot. Crystallography parameters for the crystal structures are shown in Extended Data Table 1. The Ramachandran plots show that, in all structures, >96% of residues fall into favoured regions, and the others into allowed regions. No Ramachandran outliers were observed. The refined structures were processed in Maestro (Schrodinger) using the protein preparation wizard, including the 'import and process' followed by the 'refine/optimize' functions (the default settings were used for each step). Key polar contacts were assigned using the default parameters in Maestro and confirmed in Pymol.

In all structures, the asymmetric unit (P212121) contained two molecules of KRAS and two molecules of CYPA, comprising two KRAS–RMC-7977–CYPA tri-complex promoter pairs (A/B and C/D, where A and C represent KRAS, and B and D represent CYPA). The C and D chains had higher flexibility across structures. In the GMPPNP-bound KRAS(G12D) tri-complex structure, the A/B promoter had a well-defined electron density corresponding to the nucleotide γ-phosphate in KRAS. In the C/D promoter, the density for the γ-phosphate was less-well defined, with two possible orientations (of a similar probability): one in the usual outward position and another in an inward (alternative) position. The GDP·AlF_3-loaded KRAS(G12C/A/S) tri-complex pairs had well-defined densities for the $AlF_3{\cdot}H_2O_{nu}$ moiety, enabling confident placement between Gln61 and Thr35. This orientation was similar to the only available transition-state structure of RAS (that is, WT RAS in a complex with GAP RASA1; PDB: 1WQ1). None of the GDP·AlF_3-loaded KRAS(G12D) tri-complex pairs had an electron density that would enable mapping of AlF_3 in its typical position (between Gln61 and Thr35). Nevertheless, in both promoters, the mutant aspartate (Asp12) had rotated inwards to clash with and occupy the typical space of AlF_3—a rotation that was distinct from the orientation of Asp12 in the GNPPNP-bound structures. The affinity of RMC-7977–CYPA for KRAS–GDP is very weak, suggesting that AlF_3 must have dissociated after the KRAS(G12D)-GDP·AlF_3–RMC-7977–CYPA tri-complex crystals had formed. One of the G12D promoters (C/D) contained an inward-placed electron density that could potentially represent AlF_3 (a position overlapping with the alternatively placed γ-phosphate from above). We could not reliably map any KRAS side chains, waters or magnesium to this density. The alternatively placed AlF_3 displayed a non-planar geometry, resembling the configuration of the guanosine phosphates. However, the possibility that this density represents the native γ-phosphate is unlikely, given the conditions used to generate and isolate the tri-complex crystals. To the extent that the resolution of our structures allows such an inference, the geometry of AlF_3 in the G12C model also deviated from planar (dihedral angle of 12° as compared to 17° for the putative AlF_3 in KRAS(G12D)). In KRAS(G12C), the distance between the closest fluoride atom of AlF_3 to the thiol oxygen was 2.5 Å, whereas, in KRAS(G12D), the distance between the closest fluoride to the carboxyl oxygen was 1.9 Å, suggesting a potential clash or interaction between these atoms. Dedicated studies are needed to address these possibilities and to determine the exact positioning of the $AlF_3{\cdot}H_2O_{nu}$ moiety in the transition state of KRAS(G12D). Nevertheless, the data presented here clearly demonstrate the rotation of the mutant aspartate side chain towards the catalytic core of KRAS and support an effect by its carboxyl group on the ability of drug bound CYPA to stimulate GTP hydrolysis by KRAS(G12D) in a mutant-specific manner.

Nucleotide loading

Recombinant RAS proteins used in GTPase activity assays, transition-state complex detection assays and pull-down assays were

exchanged into the indicated nucleotides as follows. In brief, 100 µl reactions containing 50 µM purified RAS and 5 mM nucleotide were incubated for 10 min at 30 °C in nucleotide loading buffer (10 mM EDTA, 50 mM HEPES pH 7.5, 50 mM NaCl). Loading reactions were then allowed to cool on ice for 5 min and completed by adding a final concentration of 20 mM $MgCl_2$. Nucleotide-loaded protein was then buffer-exchanged into the appropriate downstream assay buffer using a Zeba Spin Desalting Column (Thermo Fisher Scientific), aliquoted and snap-frozen in liquid nitrogen.

GTPase assays

Continuous hydrolysis assay. In vitro detection of orthophosphate release from the hydrolysis of GTP was measured in real time using the phosphate sensor assay (Life Technologies). In brief, the hydrolysis reaction was carried out in 384-well low volume assay plates (Corning) containing GTP-loaded RAS (1.5 µM) and 3 µM phosphate sensor protein in reaction buffer (20 mM HEPES pH 7.5, 50 mM NaCl, 1.5 mM $MgCl_2$, 1 mM TCEP). The reactions were performed with or without 10 µM CYPA and/or 10 µM TCI unless otherwise stated. Fluorescence of the bacterially derived phosphate-binding protein modified with a fluorophore (excitation, 400 nm; emission, 450 nm) was recorded on the SpectraMax iD5 plate reader (Molecular Devices) every 30 or 60 s for 90 min at 30 °C. Raw fluorescence values were background-subtracted and converted to µM units using a PO_4 standard. Kinetic constants were obtained by fitting the data to a one-phase association curve in GraphPad Prism 10.

[γ^{33}P]GTP hydrolysis assay. RAS proteins (0.6 µM) were reacted with 0.04 µM [γ^{33}P]GTP (3,000 Ci mmol^{-1}; American Radiolabeled Chemicals) in 50 µl loading buffer (50 mM HEPES, pH 7.5, 50 mM NaCl, 1 mM DTT, 0.1 mM EGTA, 10 mM EDTA and 0.1 mg ml^{-1} BSA) for 10 min at 30 °C as described previously[16]. Loading reactions were stopped by placing on ice and adding $MgCl_2$ to a final concentration of 20 mM and diluted with a total volume of 300 µl with hydrolysis buffer (25 mM HEPES pH 7.5, 50 mM NaCl, 1 mM DTT, 1 mM $MgCl_2$ and 0.1 mg ml^{-1} BSA). The GTPase assays were performed at 30 °C in 50 µl mixtures containing 50 nM of loaded KRAS in hydrolysis buffer with 500 nM RMC-7977 or DMSO control and 0–500 nM CYPA protein. After 2 h, the reactions were stopped with the addition of 150 µl ice-cold hydrolysis buffer and immediately filtering through 0.45 µm nitrocellulose membrane filters. The filters were washed three times with 0.2 ml of ice-cold hydrolysis buffer, air dried and processed by autoradiography.

Transition-state complex assay

For the detection of transition-state complex formation, mant-GDP-loaded KRAS, CYPA and inhibitors were incubated in buffer (50 mM HEPES pH 7.5, 50 mM NaCl, 2 mM $MgCl_2$ and 1 mM TCEP, 60 µM $AlCl_3$ and 25 mM NaF) at 25 °C, as previously described[34]. The reactions were dispensed in triplicate (20 µl) into low-volume 384-well assay plates and the fluorescence emission spectrum (excitation, 366 nm; emission, 400–550 nm in 2 nm steps) was recorded on the SpectraMax iD5 plate reader (Molecular Devices). Fluorescence was normalized: [((sample − buffer)− baseline)/baseline] to record the fold change over the baseline and set the baseline to zero. Analysis of fluorescence shift with titration was calculated using the area under the curve from 414 to 450 nm.

Immunoblotting and pull-downs

Whole-cell lysates for immunoblot analysis were prepared using lysis buffer (50 mM Tris-HCl (pH 8.0), 150 mM NaCl, 1% IGEPAL CA-630, 10% glycerol, 2 mM EDTA) supplemented with Halt protease and phosphatase inhibitor cocktail (Thermo Fisher Scientific). The lysates were cleared by centrifugation and the protein concentration was quantified using the Pierce BCA Protein Assay kit (Thermo Fisher Scientific). Cleared lysates were prepared in 1× Laemmli buffer and heated at 95 °C for 5 min. Then, 15–30 µg of total protein was loaded per well of precast NuPAGE gels (Life Technologies) and separated by SDS–PAGE using standard procedures.

For immunoblot detection, proteins resolved by SDS–PAGE were transferred onto nitrocellulose membranes. Membranes were blocked using 5% skimmed milk in TBST buffer for 1 h and incubated with the appropriate primary antibodies overnight. Detection was performed using HRP-linked secondary antibodies and developed with Pierce ECL substrate (Thermo Fisher Scientific) and X-ray films. Unprocessed SDS–PAGE and immunoblot images can be found in Supplementary Fig. 1. Antibody information is provided in Supplementary Table 1. Densitometry analyses were performed using Fiji[35].

For the detection of RAS–CYPA interaction by GST pulldown (PD), recombinant purified proteins (1 µM GDP- or GMPPNP-loaded GST–KRAS(G12D) and 1 µM CYPA) were incubated in PD buffer (12.5 mM HEPES pH 7.5, 75 mM NaCl, 2 mM $MgCl_2$, 0.5 mM TCEP) with 10 µM RMC-7977 and 20 µl Glutathione Sepharose 4B beads (Cytiva) for 2 h at 4 °C with end-over-end rotation. After incubation, beads were washed three times with PD buffer. Proteins were eluted using 2× Laemmli buffer and detected by SDS–PAGE as described above.

Nucleotide exchange

SOS1-mediated exchange of GDP to GTP-DY-647P1 was measured by homogeneous time-resolved fluorescence (HTRF) as previously described[17]. Briefly, 20 nM GDP-loaded GST-tagged KRAS(G12D) protein premixed with anti-GST-Tb antibody was incubated with 10 µM CYPA and inhibitors for 1 h at room temperature in buffer containing 20 mM HEPES pH 7.4, 150 mM NaCl, 5 mM $MgCl_2$, 1 mM DTT, 0.05% BSA, 0.0025% NP40. Then, 0.15 µM GTP-DY-647P1 and 12.5 nM SOS1 (amino acids 564–1049) were added to reaction wells to initiate the exchange reaction. The HTRF signal was measured on the PHERAstar (BMG Labtech) system.

Animal studies

All procedures related to animal handling, care and treatment were conducted in compliance with all applicable regulations and guidelines of the Memorial Sloan Kettering Cancer Center Institutional Animal Care and Use Committee (IACUC) (protocol: 18-05-007), as previously described[15,36].

PDX models. Tumour samples were collected from patients at Memorial Sloan Kettering Hospital with informed consent obtained in all cases (IRB protocols 06-107, 12-245 and 20-059). To generate the PDX models, cell suspensions from tumour tissue was mixed with Matrigel (BD Biosciences) and injected subcutaneously into the flanks of immunodeficient NSG mice and monitored for tumour growth as described previously[37]. Mice were group-housed under pathogen-free and controlled environmental conditions (21 ± 1.5 °C temperature, 55 ± 10% humidity and a 12 h–12 h light–dark cycle). Genetic alterations in established PDX models were verified using the MSK-IMPACT[38] platform. To assess the antitumour effect of TCIs, mice bearing PDX tumours were randomized into treatment groups (n = 5 mice per group) and treated with RMC-7977 (10 mg per kg orally) or vehicle (DMSO:PEG400:Solutol:H_2O, 10:20:10:60) for 5 days per week. Treatment began when the tumours reached 100–150 mm^3 in size and the experiments were terminated when tumours reached a maximum size of 1,500 mm^3. The tumour volume was measured in control and treated groups using callipers in a non-blinded manner by a research technician who was not aware of the objectives of the study.

Cell lines and culture conditions

All human cell lines were obtained from the American Type Culture Collection (ATCC). Cells were cultured in Dulbecco's modified Eagle's medium (DMEM), RPMI-1640 or DMEM/F12 supplemented with 10% fetal bovine serum (FBS) according to the ATCC recommendations.

All of the cell lines tested negative for mycoplasma. Validation procedures are as described by the manufacturer. Cells were grown in a humidified incubator with 5% CO_2 at 37 °C.

Live-cell RAS–RAF and RAS–CYPA sensors

KRAS, NRAS and HRAS variants were cloned into the NanoBiT vector 1.1 (Promega) and CYPA or the RBD domain of CRAF (amino acids 52–131) were cloned into the NanoBiT vector 2.1 (Promega). Then, 2×10^4 HEK293T cells were seeded on poly-D-lysine-coated (Thermo Fisher Scientific) 96-well assay plates. Cells were transfected with equal amounts of RAS mutant vector and CYPA or CRAF-RBD vectors using JetOPTIMUS (Polyplus) according to the manufacturer's instructions. For the measurement of RAS–CYPA complex formation as a function of inhibitor concentration, the cells were treated with RMC-7977 or DMSO for 2 h, NanoGlo luciferase substrate (Promega, N2011) was added, and the activity of reconstituted NanoBiT luciferase was detected in a GloMax plate luminometer (Promega). For the measurement of RAS–CYPA or RAS–RBD binding as a function of time, cells were exchanged into cell culture medium containing Nano-Glo Endurazine live-cell substrate (Promega) and allowed to equilibrate at 37 °C for 1 h. Cells were then transferred to a SpectraMax iD5 plate reader (Molecular Devices) equilibrated at 37 °C to measure NanoBiT luminescence before and after inhibitor treatment.

Reporting summary

Further information on research design is available in the Nature Portfolio Reporting Summary linked to this article.

Data availability

All data are available in the Article and its Supplementary Information. Crystal structures have been deposited at the Protein Data Bank under accession codes 9BHO, 9BHP, 9BHQ, 9BGH, 9BI1 and 9BI2. Source data are provided with this paper.

26. Otwinowski, Z. & Minor, W. Processing of X-ray diffraction data collected in oscillation mode. *Methods Enzymol.* **276**, 307–326 (1997).
27. McCoy, A. J. et al. Phaser crystallographic software. *J. Appl. Crystallogr.* **40**, 658–674 (2007).
28. Welsch, M. E. et al. Multivalent small-molecule pan-RAS inhibitors. *Cell* **168**, 878–889 (2017).
29. Fraser, J. S. et al. Hidden alternative structures of proline isomerase essential for catalysis. *Nature* **462**, 669–673 (2009).
30. Long, F. et al. AceDRG: a stereochemical description generator for ligands. *Acta Crystallogr. D* **73**, 112–122 (2017).
31. Moriarty, N. W., Grosse-Kunstleve, R. W. & Adams, P. D. Electronic Ligand Builder and Optimization Workbench (eLBOW): a tool for ligand coordinate and restraint generation. *Acta Crystallogr. D* **65**, 1074–1080 (2009).
32. Emsley, P. & Cowtan, K. Coot: model-building tools for molecular graphics. *Acta Crystallogr. D* **60**, 2126–2132 (2004).
33. Liebschner, D. et al. Macromolecular structure determination using X-rays, neutrons and electrons: recent developments in Phenix. *Acta Crystallogr. D* **75**, 861–877 (2019).
34. Mittal, R., Ahmadian, M. R., Goody, R. S. & Wittinghofer, A. Formation of a transition-state analog of the Ras GTPase reaction by Ras-GDP, tetrafluoroaluminate, and GTPase-activating proteins. *Science* **273**, 115–117 (1996).
35. Schindelin, J. et al. Fiji: an open-source platform for biological-image analysis. *Nat. Methods* **9**, 676–682 (2012).
36. Zhao, Y. et al. Diverse alterations associated with resistance to KRAS(G12C) inhibition. *Nature* **599**, 679–683 (2021).
37. Xue, Y. et al. An approach to suppress the evolution of resistance in $BRAF^{V600E}$-mutant cancer. *Nat. Med.* **23**, 929–937 (2017).
38. Cheng, D. T. et al. Memorial Sloan Kettering—Integrated Mutation Profiling of Actionable Cancer Targets (MSK-IMPACT): a hybridization capture-based next-generation sequencing clinical assay for solid tumor molecular oncology. *J. Mol. Diagn.* **17**, 251–264 (2015).

Acknowledgements We thank M. Holderfield, D. Wildes and J. Smith for their insights on this study; N. Pavletich and C. Lima for their insights on the crystal structures; and M. Mroczkowski for discussing this work throughout its stages and for reviewing the manuscript. P.L. is supported in part by the NIH/NCI (1R01CA23074501, 1R01CA23026701A1, 1R01CA279264-01 and 1P01CA129243), The Pew Charitable Trusts, the Damon Runyon Cancer Research Foundation, the Pershing Square Sohn Cancer Research Alliance, and the Center for Experimental Therapeutics, the Josie Robertson Investigator Program and the Support Grant-Core Grant program (P30 CA008748) at Memorial Sloan Kettering Cancer Center. A.C.-N. is a Berger Foundation Fellow of the Damon Runyon Cancer Research Foundation (DRG, 2513-24). D.J.R. was supported by a Medical Scientist Training Program grant from the National Institute of General Medical Sciences of the National Institutes of Health under award number T32GM152349 to the Weill Cornell/Rockefeller/Sloan Kettering Tri-Institutional MD-PhD Program.

Author contributions P.L. conceived and supervised the study. A.C.-N., Y.P. and P.L. designed experiments and analysed data. A.C.-N., F.H., D.J.R., A.V., B.S. and S.F. performed cell-based and/or biochemical experiments. Y.P. and Y.G. performed crystallization studies. A.C.-N. and E.d.S. performed in vivo studies. A.C-N., Y.P. and P.L. were the main writers of the manuscript. All of the other authors reviewed and edited the manuscript.

Competing interests P.L. is listed as an inventor on patents filed by MSKCC regarding treatment of KRAS- or BRAF-mutant cancers; reports grants to his institution from Revolution Medicines, Amgen, Mirati and Boehringer Ingelheim; and reports consulting fees or honoraria from Black Diamond Therapeutics, AmMax, OrbiMed, PAQ-Tx, Repare Therapeutics, Boehringer Ingelheim, Menarini Group and Revolution Medicines, as well as membership on the scientific advisory board of Frontier Medicines, Ikena, Biotheryx and PAQ-Tx (consulting fees and equity in each). The other authors declare no competing interests.

Additional information

Supplementary information The online version contains supplementary material available at https://doi.org/10.1038/s41586-024-08283-2.

Correspondence and requests for materials should be addressed to Piro Lito.

Peer review information *Nature* thanks Channing Der, Mark Philips and the other, anonymous, reviewer(s) for their contribution to the peer review of this work.

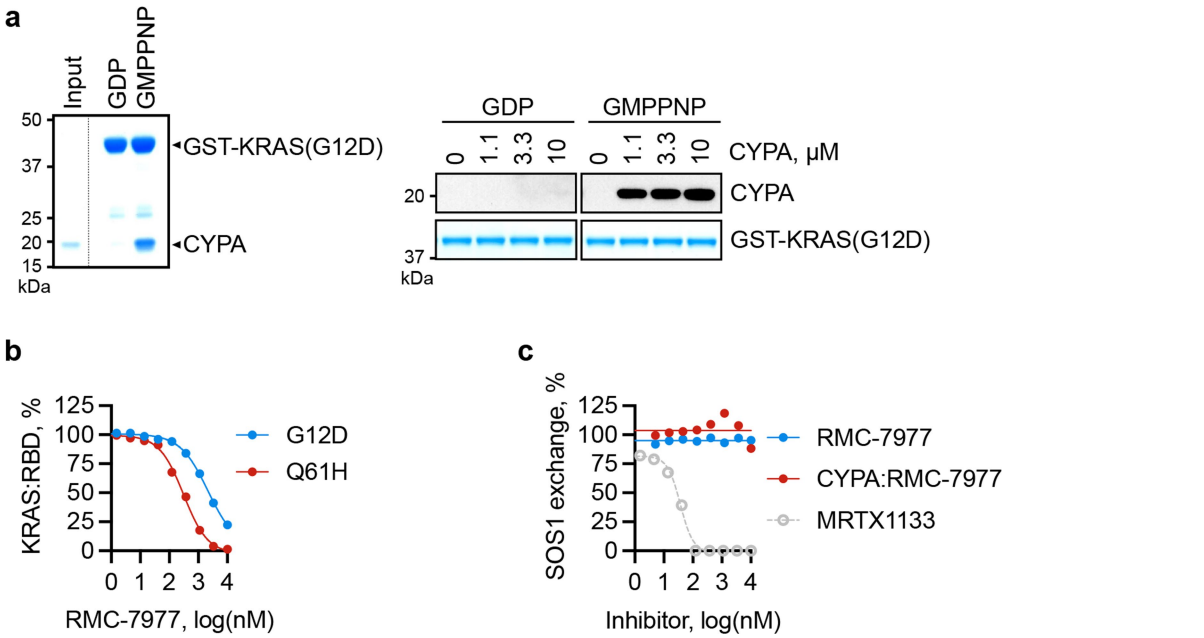

Extended Data Fig. 1 | Selective binding and inhibition of the KRAS active state. a, Pulldown of GDP, or GMPPNP-loaded GST-KRAS G12D incubated with CYPA preloaded with RMC-7977. **b**, Effect of CYPA:RMC-7977 on the complex between the indicated GMPPNP-loaded KRAS variant and the RAS-binding domain (RBD) of CRAF. **c**, KRAS G12D was subjected to an exchange reaction (GDP to GTP-DY-647P1) in the presence of SOS1 and increasing concentrations of TCI (with or without 10 μM CYPA) or the inactive-state selective G12D inhibitor MRTX1133. A representative of two independent repeats is shown for **a**-**c**.

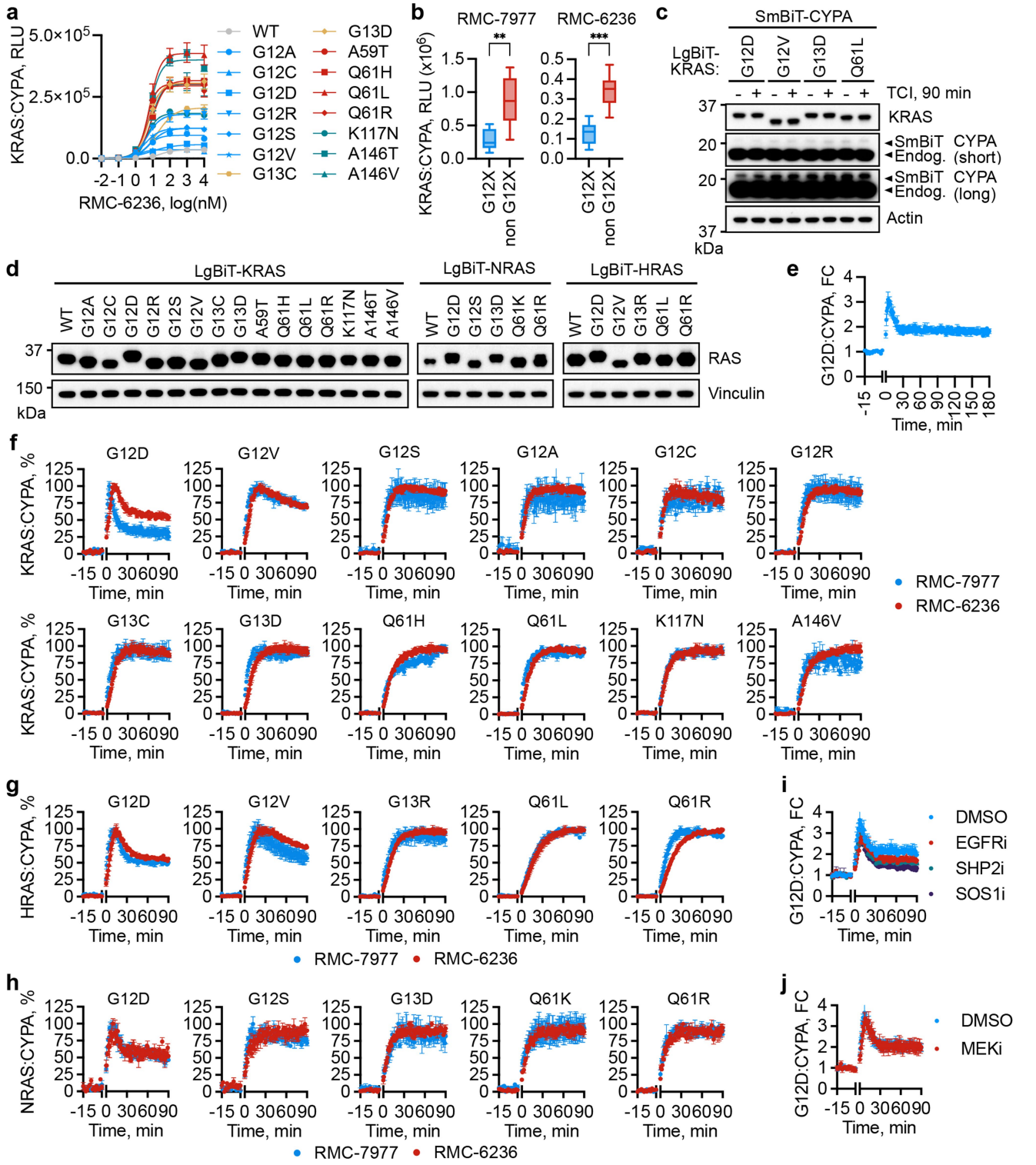

Extended Data Fig. 2 | Propensity for drug induced CYPA complex formation across RAS mutants. a,b, Live cells expressing a split luciferase reporter detecting the complex between CYPA and the indicated KRAS variants were treated with RMC-6236 or RMC-7977 for 2h (n = 3 per variant, **a**: mean ± s.e.m., **b**: interquartile range and Tukey whiskers). **c**, Immunoblot analysis of extracts from HEK293T cells expressing the indicated split luciferase-tagged constructs, either after RMC-7977 treatment (**c**) or at baseline (**d**). **e**, KRAS G12D:CYPA binding reaches plateau at ~30 min. **f-g**, Detection of CYPA in complex with the indicated KRAS (**f**), HRAS (**g**), NRAS (**h**) mutants expressed in cells treated with TCI (100 nM, added at time 0). **i,j**, Cells were treated with 100 nM RMC-7977 and either gefitinib (EGFRi, 5 μM, **i**), RMC-4550 (SHP2i, 10 μM, **i**), BI-3406 (SOS1i, 10 μM, **i**), trametinib (MEKi, 100 nM, **j**) or DMSO at time 0. The effects on KRAS G12D:CYPA steady state levels are shown. SmBiT: small bit luciferase, LgBiT: large bit luciferase. **e-j**: n = 3 biological replicates, mean ± s.e.m.

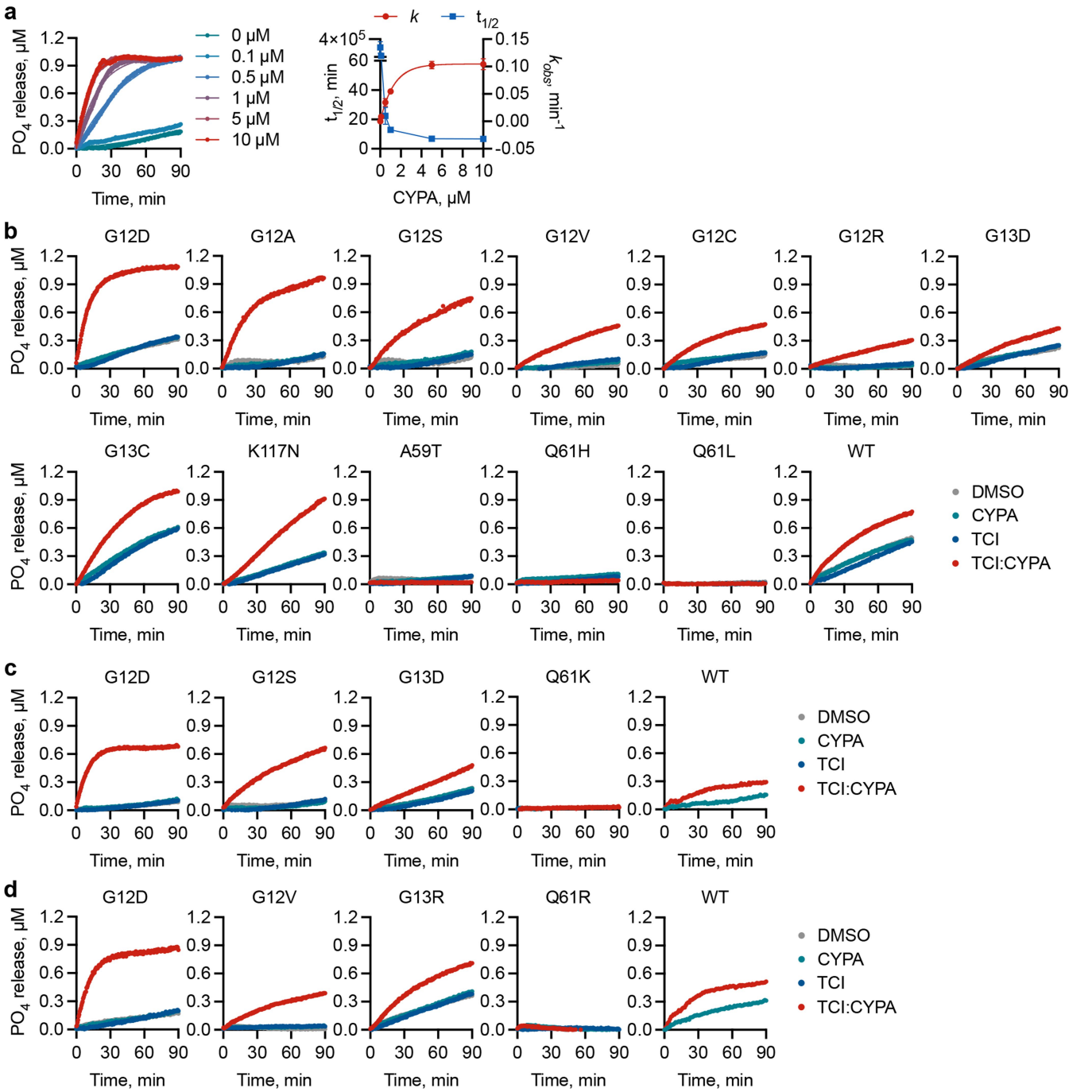

Extended Data Fig. 3 | Pharmacologic enhancement of the GTPase activity of select RAS variants. a, The effect of increasing concentrations of the binary CYPA:RMC-7977 complex on GTP hydrolysis by KRAS G12D was determined as in Fig. 2a. The data were then fit to a one-phase association curve. A representative reaction over time (left) and the kinetic parameters (right) of three independent experiments are shown (mean ± s.e.m.). **b**-**d**, The effect of CYPA, RMC-7977 alone or as a binary complex, on the GTPase activity of the indicated KRAS (**b**), NRAS (**c**) or HRAS (**d**) variants. A representative of two independent experiments for each RAS variant is shown in **b**-**d**.

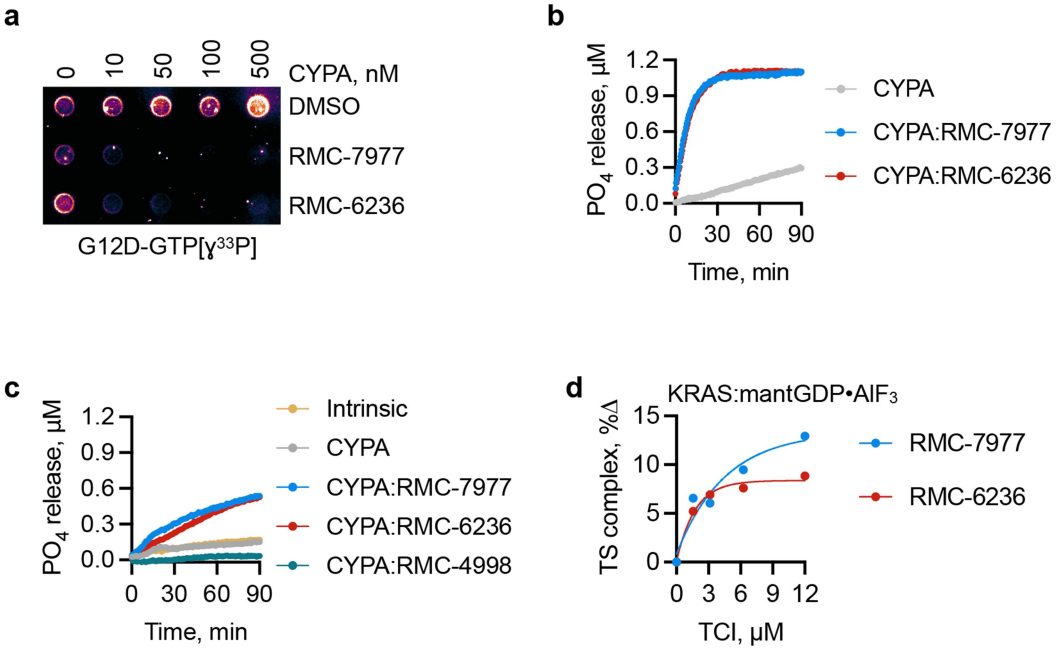

Extended Data Fig. 4 | Effect of various tri-complex inhibitors on GTP hydrolysis by KRAS. a,**b**, KRAS G12D was reacted with the indicated CYPA complexes to determine the effect on hydrolysis either relying on either [γ^{33}P]GTP (**a**) or a phosphate sensor and non-radiolabeled GTP (**b**). **c**, As in **b** but KRAS G12C was used instead of KRAS G12D. **d**, Purified KRAS G12D loaded with mantGDP (mGDP) and AlF_3 was reacted with increasing concentrations TCI-bound CYPA. The formation of a transition state complex was detected by fluorescence as in Fig. 2c. A representative of two independent repeats is shown for **a**-**d**.

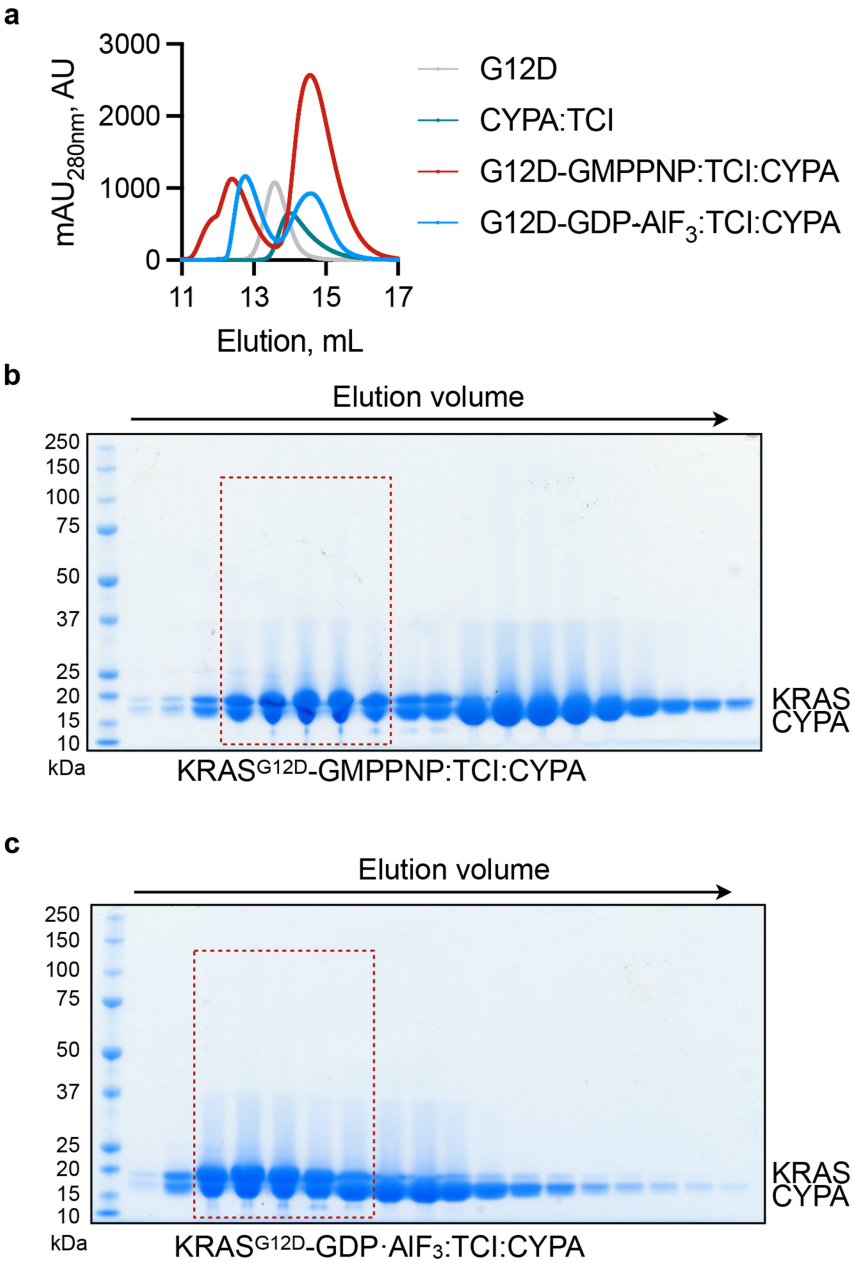

Extended Data Fig. 5 | Isolation and crystallization of ground and transition state complexes. a-c, Purified KRAS G12D loaded with the indicated nucleotides was reacted with CYPA bound to RMC-7977 and the mixture was separated by size exclusion chromatography. The optical density of the elution fractions is shown in **a**. Eluted fractions from the KRAS ground state (**b**, GMPPNP-bound) or transition state (**c**, GDP·AlF_3-bound) reactions were subjected to SDS-PAGE followed by Coomassie Brilliant Blue (CBB) staining. A representative of two independent repeats are shown in **b** and **c**. The fractions containing the complex are indicated by the dotted line. **d**,**e**, Representative crystals of the ground state (**d**) or transition state (**e**) complexes that were established using the hanging drop method.

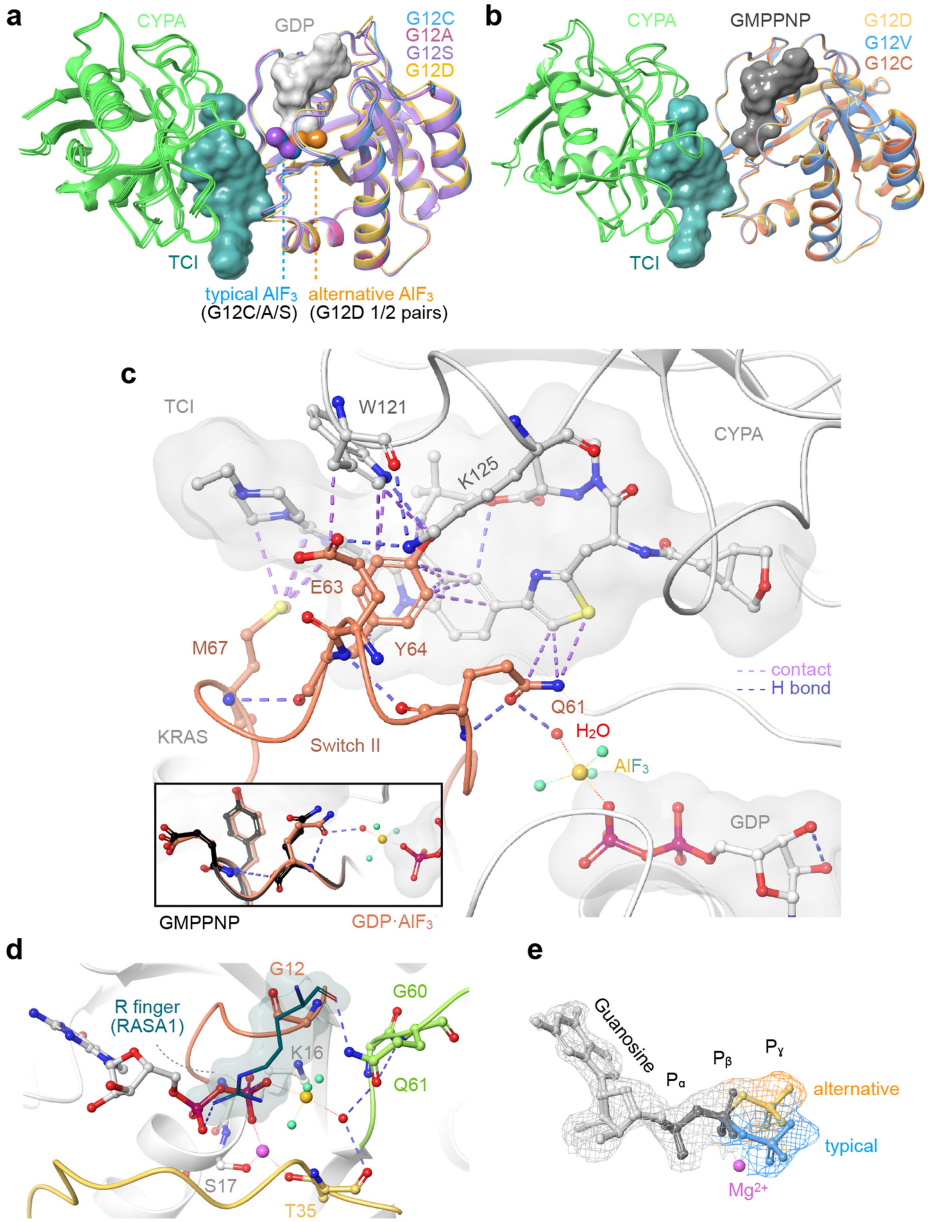

Extended Data Fig. 6 | Features of the GMPPNP- or GDP·AlF_3-loaded KRAS variants in complex with CYPA. a,**b**, Superimposed tertiary structures of KRAS mutants loaded with either GMPPNP (ground state mimetic, **a**) or GDP·AlF_3 (transition state mimetic, **b**) bound to the tri-complex inhibitor RMC-7977 and CYPA. **c**, Interactions of CYPA:RMC-7977 with the indicated switch II residues in GDP·AlF_3-loaded KRAS G12C. Inset: the rotation of the Q61 side chain leading to the carbonyl oxygen being orientated towards the nucleophilic water in the GDP·AlF_3-bound state. **d**, Wild type HRAS in a transition state complex with the GAP domain of RASA1 (from 1WQ1). Note the GAP arginine (R) finger-mediated charge stabilization of the α and β phosphates (guanidino group) and the coordination of Q61 (backbone carbonyl). **e**, 2Fo-Fc map of GMPPNP-bound KRAS G12D with two plausible occupancies for the γ-phosphate (P).

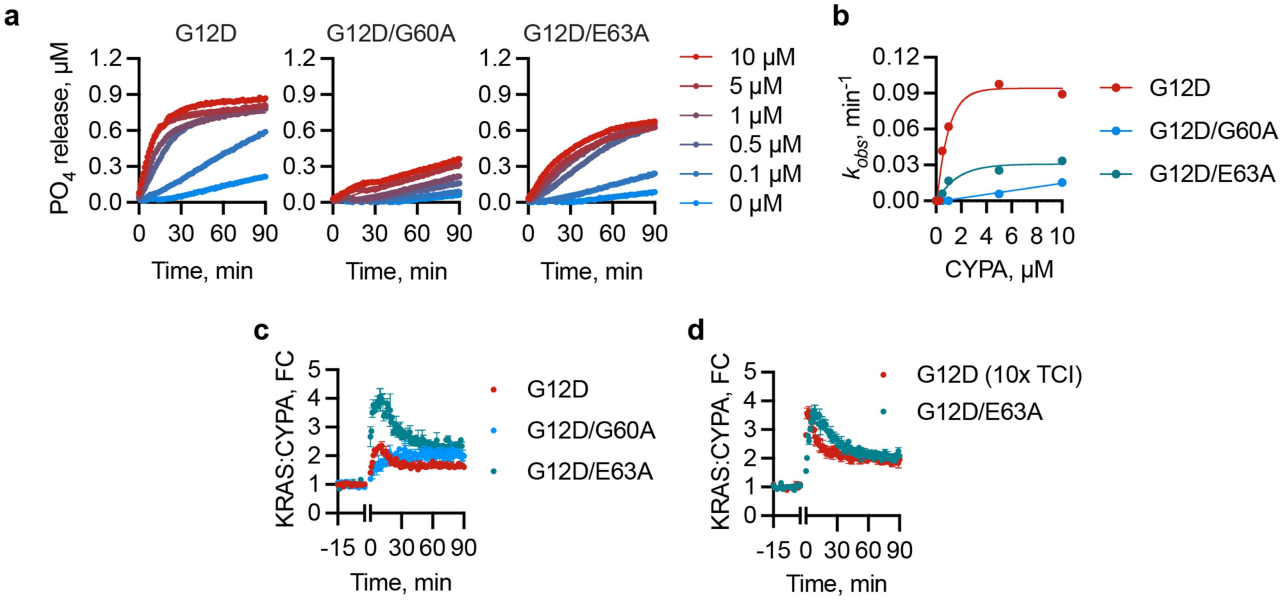

Extended Data Fig. 7 | KRAS amino acids that contribute to tri-complex induced hydrolysis. a, The effect of increasing concentrations of CYPA on GTP hydrolysis by the indicated KRAS variants (RMC-7977: 10 µM throughout). A representative of n = 2 independent experiments for each variant is shown. **b**, Data from (**a**) were fitted to a one-phase association curve to obtain the rate constant (*k*) as a function of CYPA concentration. **c**, The complex of CYPA and the indicated KRAS mutants was induced by 100 nM RMC-7977 detected in live cells (n = 3 biological replicates, mean±s.e.m.). **d**, As in **c** but 0.1 µM RMC-7977 was used for G12D/E63A and 1 µM for G12D to account for the higher KRAS:CYPA binding level of the double mutant (n = 3 biological replicates, mean ± s.e.m.). Note the slower dissociation of G12D/E63A from CYPA in live cells, which is consistent with the slower tri-complex induced hydrolysis in the double mutant, as shown in **a** and **b**.

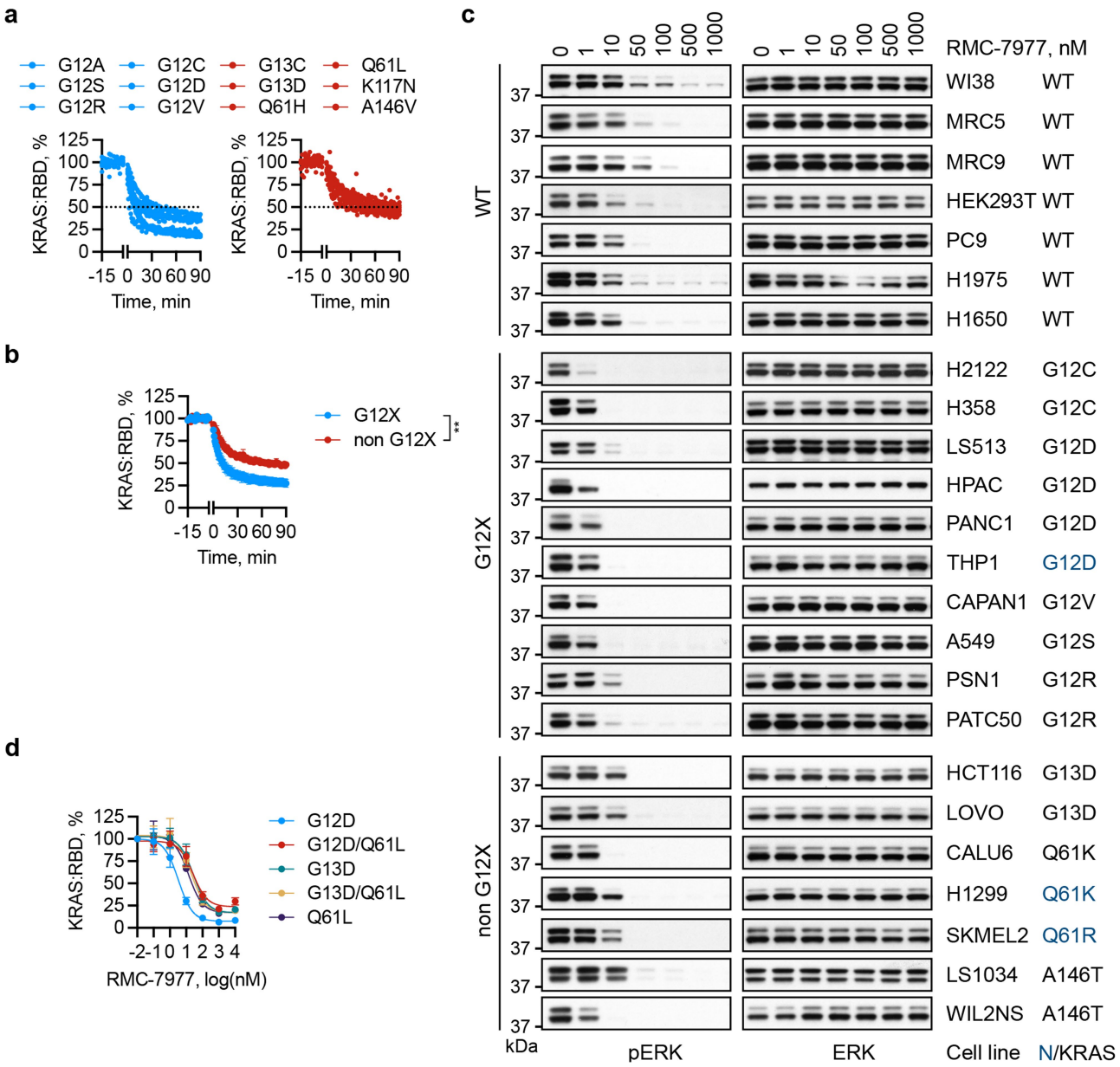

Extended Data Fig. 8 | Inducing hydrolysis enhances target inhibition despite impairing CYPA complex formation. a,**b**, HEK293T cells expressing SmBiT-tagged CRAF-RBD along with the indicated LgBiT-KRAS variants were treated with 100 nM RMC-7977 at time 0. Live cells were analysed for drug-induced complex formation by measuring the activity of reconstituted luciferase. (n = 3 replicates per variant, **a**: mean for each variant, **b**: mean ± s.e.m., **p = 0.0022, two-way ANOVA). **c**, Immunoblot detection of phosphorylated ERK in extracts from cells treated with RMC-7977 for 2 h. **d**, Interaction of the CRAF-RBD with the indicated single or double KRAS mutants expressed in cells that were treated with RMC-7977 for 2h.

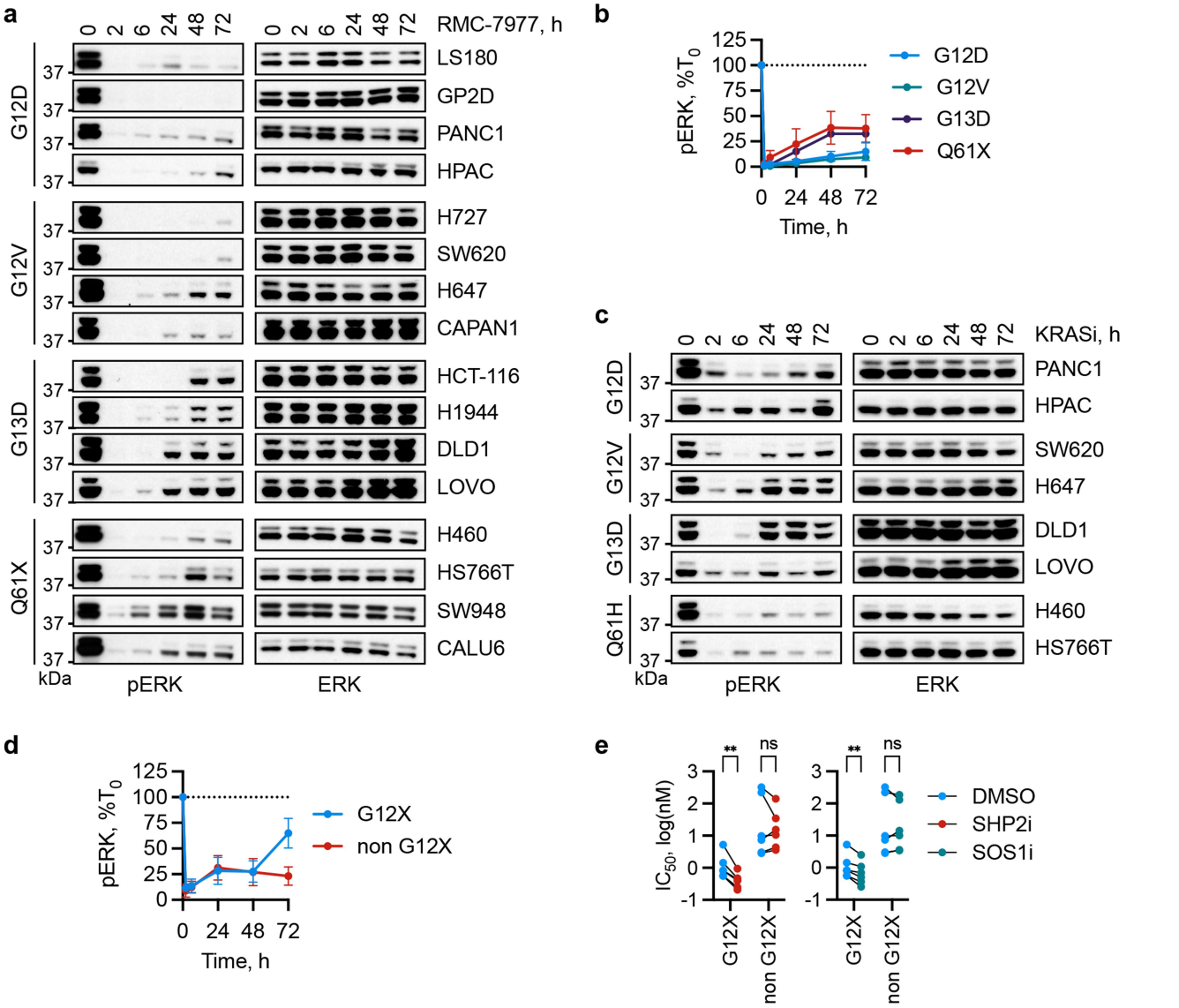

Extended Data Fig. 9 | Differences in durability of inhibition across KRAS mutant models. a,**b**, Extracts from cells that were treated with RMC-7977 over time (200 nM) were analysed by immunoblotting to determine the effect on ERK activation. Densitometric quantification is shown in **b** (n = 4 cell lines per allele). **c**,**d**, As in **a** and **b**, but the indicated cell lines (n = 2 cell lines per allele) were treated with an inactive state selective pan KRAS inhibitor (BI-2865, 1 μM). In **b** and **d**, datapoints denote mean ± s.e.m. A representative of two independent repeats are shown in **a** and **c**. **e**, KRAS mutant cell lines were treated with RMC-7977 with or without 1 μM SHP2i (RMC-4550) or SOS1i (BI-3406) for 72h to determine the effect on viability using ATP glow and compare the the changes in IC_{50}s (n = 6 cell lines per group, mean of 3 biological replicates per cell line is shown, **p = 0.0031 (left) and **p = 0.0096 (right), two-tailed paired t test and Holm-Šídák test to correct for multiple comparisons). Albeit modest, the effect of both SHP2i and SOS1i combinations was restricted to G12X models, a finding that supports the mutant selective stimulation of GTP hydrolysis by RMC-7977.

Extended Data Table 1 | Crystallographic data collection and refinement statistics

	G12D-GMPNNP	G12D-GDP·AlF_3	G12C-GMPNNP	G12C-GDP·AlF_3	G12A-GDP·AlF_3	G12S-GDP·AlF_3
PDB ID	9BI1	9BGH	9BI2	9BHP	9BHQ	9BHO
Data collection[1,2,3]						
Space group	P 21 21 21	P 21 21 21	P 21 21 21	P 21 21 21	P 21 21 21	P 21 21 21
Cell dimensions						
a, *b*, *c* (Å)	65.52, 82.05, 127.90	65.48, 81.79, 127.83	65.13, 81.55, 128.18	65.46, 82.65, 127.83	65.61, 83.31, 127.69	65.29, 83.05, 127.63
α, β, γ (°)	90, 90, 90	90, 90, 90	90, 90, 90	90, 90, 90	90, 90, 90	90, 90, 90
Resolution (Å)	1.65	1.65	2.15	2.10	1.90	1.890
R_{sym} or R_{merge}	0.107 (0.692)	0.106 (0.798)	0.199 (0.767)	0.105 (0.779)	0.155(0.829)	0.106 (0.701)
I / σI	24.0 (2.235)	27.2 (1.522)	14.24 (1.89)	15.71 (1.56)	11.37 (1.279)	16.167 (1.367)
Completeness (%)	92.27 (97.18)	92.94 (98.43)	98.21 (97.67)	98.57 (96.17)	93.10 (78.41)	96.46 (85.40)
Redundancy	8.0 (5.7)	8.0 (6.0)	6.6 (6.9)	7.0 (5.1)	5.4 (2.5)	7.5 (4.1)
Refinement						
Resolution (Å)	1.65	1.65	2.15	2.10	1.90	1.89
No. reflections	79805 (7964)	77261 (8098)	37553 (3600)	40660 (3940)	52063 (4330)	54157 (4719)
R_{work} / R_{free}	0.2179/0.2589	0.2174/0.2505	0.1751/0.2355	0.2114/0.2520	0.1930/0.2320	0.1848/0.2176
No. atoms						
Protein	5198	5225	5194	5117	5225	5289
Ligand/ion	336	130	336	134	254	254
Water	618	485	328	266	376	481
B-factors						
Protein	34.58	37.24	31.10	41.97	31.12	30.03
Ligand/ion	27.98	28.12	24.57	31.81	24.19	21.78
Water	40.24	37.91	32.26	37.54	32.67	32.90
R.m.s. deviations						
Bond lengths (Å)	0.011	0.015	0.011	0.009	0.011	0.013
Bond angles (°)	1.115	1.40	1.07	0.66	0.73	1.00

[1]Each dataset was obtained from a single crystal.

[2]Values in parentheses are for highest-resolution shell.

[3]Each column represents tri-complex structures of CYPA, RMC-7977 and the indicated nucleotide loaded KRAS variants.

nature portfolio

Corresponding author(s): Piro Lito, MD, PhD

Last updated by author(s): Oct 5, 2024

Reporting Summary

Nature Portfolio wishes to improve the reproducibility of the work that we publish. This form provides structure for consistency and transparency in reporting. For further information on Nature Portfolio policies, see our Editorial Policies and the Editorial Policy Checklist.

Statistics

For all statistical analyses, confirm that the following items are present in the figure legend, table legend, main text, or Methods section.

n/a	Confirmed	
☐	☒	The exact sample size (*n*) for each experimental group/condition, given as a discrete number and unit of measurement
☐	☒	A statement on whether measurements were taken from distinct samples or whether the same sample was measured repeatedly
☐	☒	The statistical test(s) used AND whether they are one- or two-sided *Only common tests should be described solely by name; describe more complex techniques in the Methods section.*
☒	☐	A description of all covariates tested
☐	☒	A description of any assumptions or corrections, such as tests of normality and adjustment for multiple comparisons
☐	☒	A full description of the statistical parameters including central tendency (e.g. means) or other basic estimates (e.g. regression coefficient) AND variation (e.g. standard deviation) or associated estimates of uncertainty (e.g. confidence intervals)
☐	☒	For null hypothesis testing, the test statistic (e.g. *F*, *t*, *r*) with confidence intervals, effect sizes, degrees of freedom and *P* value noted *Give P values as exact values whenever suitable.*
☒	☐	For Bayesian analysis, information on the choice of priors and Markov chain Monte Carlo settings
☒	☐	For hierarchical and complex designs, identification of the appropriate level for tests and full reporting of outcomes
☒	☐	Estimates of effect sizes (e.g. Cohen's *d*, Pearson's *r*), indicating how they were calculated

Our web collection on statistics for biologists contains articles on many of the points above.

Software and code

Policy information about availability of computer code

Data collection	X-ray diffraction datasets were collected at the NSLS II 17-ID-2 (FMX) beamline.
Data analysis	The diffracted images were processed with HKL2000 (v722) and all structures were solved by molecular replacement using a previously solved structure. Model building and refinement was performed with standard protocols using CCP4 (v8.0.018), COOT (v0.9.8.93 EL), and Phenix (1.20.1-4487). The refined structures were processed in Maestro (Schrodinger, v2024-3) with the protein preparation wizard, including the 'import and process' followed by the 'refine/optimize' functions (default settings were used for each step). Key polar contacts were assigned using default parameters in Maestro and confirmed in Pymol (v2.5.5). For Western Blot analysis, Fiji (v2.14) was used. Prism 10 (GraphPad) was used to plot data, estimate IC50, and display data in graphical form.

For manuscripts utilizing custom algorithms or software that are central to the research but not yet described in published literature, software must be made available to editors and reviewers. We strongly encourage code deposition in a community repository (e.g. GitHub). See the Nature Portfolio guidelines for submitting code & software for further information.

Data

Policy information about availability of data

All manuscripts must include a data availability statement. This statement should provide the following information, where applicable:

- Accession codes, unique identifiers, or web links for publicly available datasets
- A description of any restrictions on data availability
- For clinical datasets or third party data, please ensure that the statement adheres to our policy

All data are available in the main text or the supplementary materials. Crystal structures have been deposited in PDB with accession numbers: 9BHO, 9BHP, 9BHQ, 9BGH, 9BI1 and 9BI2.

Research involving human participants, their data, or biological material

Policy information about studies with human participants or human data. See also policy information about sex, gender (identity/presentation), and sexual orientation and race, ethnicity and racism.

Reporting on sex and gender	Sex and gender were not utilized or analyzed in this manuscript as this study was not aimed at investigating sex or gender differences in cancer patients with KRAS mutations.
Reporting on race, ethnicity, or other socially relevant groupings	Racial, ethnic, or other socially relevant groupings were not utilized in this manuscript.
Population characteristics	Tumor samples were collected from lung, pancreatic, and colorectal cancer patients harboring a KRAS mutation.
Recruitment	Tumor samples were collected from patients at Memorial Sloan Kettering Hospital.
Ethics oversight	Tumor samples were collected with informed consent obtained in all cases (IRB protocols 06-107, 12-245 and 20-059).

Note that full information on the approval of the study protocol must also be provided in the manuscript.

Field-specific reporting

Please select the one below that is the best fit for your research. If you are not sure, read the appropriate sections before making your selection.

☒ Life sciences ☐ Behavioural & social sciences ☐ Ecological, evolutionary & environmental sciences

For a reference copy of the document with all sections, see nature.com/documents/nr-reporting-summary-flat.pdf

Life sciences study design

All studies must disclose on these points even when the disclosure is negative.

Sample size	For pre-clinical in vivo studies a sample size of 5 mice per cohort enables 80% power to detect an odds parameter of 14.0 for each pairwise comparison, with two-sided α level = 0.05. For all other experiments, sample sizes were not predetermined but were chosen according to the standards of the field.
Data exclusions	All data were used in statistical testing, unless otherwise specified in the text.
Replication	The experimental replicates are stated in the figure legends. All stated replicates indicate biological replicates.
Randomization	In vivo tumor growth experiments: mice were treated in a random manner with either vehicle or drug. For biochemical or in vitro experiments, randomization was not applied as it is not a standard in the field.
Blinding	Tumor growth measurements were carried out in a blinded manner by a technician who was not aware of the goals of the experiment.

Reporting for specific materials, systems and methods

We require information from authors about some types of materials, experimental systems and methods used in many studies. Here, indicate whether each material, system or method listed is relevant to your study. If you are not sure if a list item applies to your research, read the appropriate section before selecting a response.

Materials & experimental systems

n/a	Involved in the study
☐	☒ Antibodies
☐	☒ Eukaryotic cell lines
☒	☐ Palaeontology and archaeology
☐	☒ Animals and other organisms
☒	☐ Clinical data
☒	☐ Dual use research of concern
☒	☐ Plants

Methods

n/a	Involved in the study
☒	☐ ChIP-seq
☒	☐ Flow cytometry
☒	☐ MRI-based neuroimaging

Antibodies

Antibodies used

Primary (1:1000 diultion): ERK (4696, CST), pERK (9101, CST), RAS (05-516, Millipore Sigma), CYPA (2175, CST), Vinculin (13901, CST), KRAS (WH0003845M1, Sigma), Actin (4970, CST).

Secondary (1:3000 dilution): Mouse IgG HRP (7076, CST), Rabbit IgG HRP (7074, CST)

Validation

Our lab commonly uses these antibodies, which have been validated in our previous publications or in other published studies (Kim et al., Nature 2023; Schulze et al., Science 2023). Validation by the manufacturer can also be found at:

https://www.cellsignal.com/products/primary-antibodies/p44-42-mapk-erk1-2-l34f12-mouse-mab/4696
https://www.cellsignal.com/products/primary-antibodies/phospho-p44-42-mapk-erk1-2-thr202-tyr204-antibody/9101
https://www.cellsignal.com/products/primary-antibodies/cyclophilin-a-antibody/2175
https://www.cellsignal.com/products/primary-antibodies/vinculin-e1e9v-xp-rabbit-mab/13901
https://www.cellsignal.com/products/primary-antibodies/b-actin-13e5-rabbit-mab/4970
https://www.emdmillipore.com/US/en/product/Anti-Ras-Antibody-clone-RAS10,MM_NF-05-516
https://www.sigmaaldrich.com/US/en/product/sigma/wh0003845m1

Eukaryotic cell lines

Policy information about cell lines and Sex and Gender in Research

Cell line source(s)

The following cell lines were used in this study and were obtained from ATCC: HEK293T, LS180, GP2D, PANC1, HPAC, HS766T, SW948, CALU6, H460, WI38, MRC5, MRC9, PC9, H1975, H1650, H2122, H358, LS513, THP1, CAPAN1, A549, PSN1, PATC50, HCT116, LOVO, H1299, SKMEL2, LS1034, WIL2NS.

Authentication

Cell lines were obtained directly from the vendor and used in studies before 20 passages. Cell lines were not independently authenticated.

Mycoplasma contamination

All cell lines tested were negative for mycoplasma contamination.

Commonly misidentified lines
(See ICLAC register)

No commonly misidentified lines were used.

Animals and other research organisms

Policy information about studies involving animals; ARRIVE guidelines recommended for reporting animal research, and Sex and Gender in Research

Laboratory animals

Patient derived xenografts were implanted into female NOD scid gamma (NSG) mice at 6 weeks of age.

Wild animals

No wild animals were used in this study.

Reporting on sex

Studies utilized female mice.

Field-collected samples

No field-collected samples were used in this study.

Ethics oversight

All procedures related to animal handling, care and treatment were conducted in compliance with all applicable regulations and guidelines of the Memorial Sloan Kettering Cancer Center Institutional Animal Care and Use Committee (IACUC).

Note that full information on the approval of the study protocol must also be provided in the manuscript.

Plants

Seed stocks	N/A
Novel plant genotypes	N/A
Authentication	N/A